# A generalized relationship linking water balance and vegetation carbon uptake across site-to-regional scales

**Guta Wakbulcho Abeshu[1], Hong-Yi Li[1*], Mingjie Shi[2], Jack Brookshire[3], Jingyun Tang[4], Chonggang Xu[5], Nate McDowell[2,6], and L. Ruby Leung[2]**

[1] Department of Civil and Environmental Engineering, University of Houston, USA

[2]Atmospheric Sciences and Global Change Division, Pacific Northwest National Laboratory, Richland, PO Box 999, Richland, WA, 99352, USA

[3]Department of Land Resources and Environmental Sciences, Montana State University, USA

[4]Climate and Ecosystem Sciences Division, Lawrence Berkeley National Laboratory, USA

[5]Earth and Environmental Sciences Division, Los Alamos National Laboratory, USA

[6]School of Biological Sciences, Washington State University, PO Box 644236, Pullman, WA 99164-4236, USA

[*]Corresponding author: Hong-Yi Li (hongyili.jadison@gmail.com)

**Key Points:**

- A generalized relationship between monthly water balance and vegetation carbon uptake is evaluated across the U.S. catchments
- A parameter regionalization strategy is proposed based on the linkages between environmental factors and the relationship's parameters
- The relationship and its parameterization are validated across the site, catchment, and regional scales

**Abstract**

The linear relationship between gross primary productivity (GPP) and evapotranspiration (ET), evidenced by site-scale observations, is well recognized as an indicator of the close interactions between carbon and hydrologic processes in terrestrial ecosystems. However, it is not clear whether this relationship holds at the catchment scale, and if so, what are the controlling factors of its slope and intercept. This study proposes and examines a generalized GPP-ET relationship at 380 near-natural catchments across various climatic and landscape conditions in the contiguous U.S., based on monthly remote sensing-based GPP data, vegetation phenology, and several hydrometeorological variables. We demonstrate the validity of this GPP-ET relationship at the catchment scale, with Pearson's $r \geq 0.6$ for 97% of the 380 catchments. Furthermore, we propose a regionalization strategy for estimating the slope and intercept of the generalized GPP-ET relationship at the catchment scale by linking the parameter values a priori with hydrometeorological data. We validate the monthly GPP predicted from the relationship and regionalized parameters against remote-sensing based GPP product, yielding Kling-Gupta Efficient (KGE) values $\geq 0.5$ for 92% of the catchments. Finally, we verify the relationship and its parameter regionalization at 35 AmeriFlux sites with KGE $\geq 0.5$ for 25 sites, demonstrating that the new relationship is transferable across the site, catchment, and regional scales. The relationship will be valuable for diagnosing coupled water–carbon simulations in land surface and Earth system models and constraining remote-sensing based estimation of monthly ET.

# 1. Introduction

The linear relationship between gross primary productivity (GPP) and evapotranspiration (ET) has been studied by ecologists over the past decades. The relationship is considered a manifestation of the tight coupling between carbon and water fluxes via both biotic and abiotic processes and their interactions (Baldocchi, 1994; Baldocchi et al., 2001; Beer et al., 2007, 2009; Gentine et al., 2019; Law et al., 2002; Niu et al., 2011; Ponton et al., 2006; Smallman & Williams, 2019; Y. Yang et al., 2013; Zhou et al., 2014). Understanding this relationship provides valuable information on global carbon and water balance, vegetation growth, ecosystem responses to environmental changes, and the trade-off between photosynthetic carbon assimilation and concomitant transpiration (M. Huang et al., 2015; Ito & Inatomi, 2012; Keenan et al., 2013; Novick et al., 2016; Van Der Sleen et al., 2015). As such, in recent decades, the coupling between these two processes has been recognized as essential for assessing ecosystem-level response to climate variability (Baldocchi, 1994; Beer et al., 2009; Brümmer et al., 2012; Hatfield & Dold, 2019; Kuglitsch et al., 2008; Niu et al., 2011; Ponton et al., 2006; Xiao et al., 2013). Still, a better quantification of the GPP-ET relationship has been called upon to improve our understanding of the consequences of the projected future changes in temperature and precipitation regimes on ecosystem carbon and water balance (Krinner et al., 2014; Niu et al., 2011; Zhou et al., 2017).

Hydrologists view ET as a critical component of water balance at the catchment scale (Abeshu & Li, 2021; Fu, 1981; Greve et al., 2015, 2016; Ol'dekop, 1911; Pike, 1964; Sivapalan et al., 2011; Troch et al., 2009; Turc, 1954; Wang & Tang, 2014; L. Zhang et al., 2001, 2004). For instance, the Budyko curve describes the evaporative index, a ratio of long-term mean actual ET over long-term mean precipitation, as a function of climate regimes in terms of aridity index, a ratio of long-term mean potential ET over long-term mean precipitation (Budyko, 1974; Chen & Sivapalan, 2020; Choudhury, 1999; Li et al., 2014; Li & Sivapalan, 2014; Meira Neto et al., 2020; H. Yang et al., 2008; Yao & Wang, 2022; Ye et al., 2015; L. Zhang et al., 2001, 2004). Parameters of the Budyko-type formulas are closely related to vegetation dynamics at the catchment scale (Donohue et al., 2007, 2010; Wang & Tang, 2014; L. Zhang et al., 2001; S. Zhang et al., 2016, 2018). The Horton Index, defined as the ratio of ET over total wetting (water available for vaporization), has even closer linkages with a few phenological features (Abeshu & Li, 2021; Brooks et al., 2011; Horton, 1933; Sivapalan et al., 2011; Tang & Wang, 2017; Troch et al., 2009; Voepel et al., 2011). It is thus a step further in connecting catchment-scale water balance and vegetation dynamics. However, few of these hydrologic studies focus on the GPP-ET relationship within the context of catchment water balance. This motivates the first objective of this study to examine the GPP-ET relationship at the catchment scale across various climate and vegetation regimes.

Ecologists have established the coupled relationship between photosynthetic carbon assimilation and transpiration at the leaf scale (Bacon, 2004; Farquhar et al., 1989; Lloyd & Farquhar, 1994; Peters et al., 2018; Seibt et al., 2008) and between GPP and ET at the ecosystem scale (Baldocchi, 1994; Beer et al., 2009; Jiang et al., 2020; Law et al., 2002; L. Yu et al., 2022; Zhou et al., 2014, 2017) from observations. Equation (1) describes the generic GPP-ET relationship at the ecosystem scale. The slope of the relationship, $\omega$, is referred to as water use efficiency and is often estimated as the ratio of long-term mean GPP to long-term mean ET at the ecosystem scale (Beer et al., 2009). When used for estimating GPP or ET, the equation is assumed to have a zero-intercept, i.e., GPP is negligible when ET approaches zero and vice versa (Beer et al., 2007, 2010; Y. Yang et al., 2013).

$$GPP = \omega ET$$

However, it has been argued that an additional intercept term is needed for the ecosystem-scale GPP-ET relationship (Boese et al., 2017). In other words, the intercept term is not always negligible. As illustrated in Fig. 1, the zero-intercept assumption is not valid in at least three cases: 1) at cropland sites after harvest GPP is zero, but ET may not be negligible due to surface evaporation (see Nguyen & Choi, 2022); in evergreen forest-dominated ecosystems, there is a certain level of carbon assimilation even during the winter season (see Beer et al., 2007; G. Yu et al., 2008); in wetland or broadleaf forest-dominated ecosystems, significant evaporation occurs during the dormant season (see Baldocchi & Ryu, 2011). Over the past decades, many studies provided a quantitative understanding of the biotic and abiotic implications of the slope and its environmental controlling factors across vegetation types and spatial scales (Beer et al., 2009, 2010; Yulong Zhang et al., 2016; Zhou et al., 2014). However, there remains a lack of direct quantitative assessments of the slope and its linkages to climatic and environmental factors with the inclusion of the intercept term (Boese et al., 2017), let alone an understanding and assessment of the intercept term. Among the very few exceptions is a study by Boese et al. (2017) at the site scale, where they introduced various intercept options to Eqn. 1 to predict ET based on GPP at over a hundred eddy covariance sites. However, their formulation has several limitations, such as using rain-free periods only for parameter estimation and excluding the other environmental conditions that could influence the stomatal opening of plants. Furthermore, the intercept term of their best-performing model is entirely independent of any variable reflecting vegetation activity. This motivates our second objective to derive quantitative linkages between the slope and intercept of the GPP-ET relationship and climatic and environmental factors.

The linear GPP-ET relationship has been utilized to evaluate simulations by large-scale land surface or earth system models, for instance, regarding the coupling between water and carbon fluxes at the regional or global scales (M. Huang et al., 2016; Ito & Inatomi, 2012; Sun et al., 2016; S. Yang et al., 2020, 2021; Z. Yu et al., 2017). However, most global GPP simulations suffer from significant biases and uncertainties (Yahai Zhang & Ye, 2021, 2022). A recent study evaluated forty-four global GPP products (nearly thirty were model-based outputs, and the rest were observation-based) and found significant inconsistencies among model-based products for some regions, seasons, and vegetation types (Yahai Zhang & Ye, 2021). A chief reason behind these GPP simulation biases and inconsistencies is a mismatch of spatial scales, i.e., between the site scale (where process understanding has been gained from local observations) and the regional or global scales (where the models are developed and applied) (Xie et al., 2023). In the land surface or earth system models, the global domain is discretized into grids with typical grid sizes ranging from tens to thousands of $km^2$, far larger than the site scale, which is on the order of $< 1km^2$ (Pastorello et al., 2020). Such a scale mismatch often leads to large model structural uncertainty, e.g., oversimplification or poor parameterization of sub-grid heterogeneity, which is non-trivial at the typical spatial resolutions that land surface or earth system models are applied (Bonan et al., 2018; Li et al., 2011, 2013; Smallman et al., 2013; Smallman & Williams, 2019). Therefore, our third objective is to verify whether the new understanding of the GPP-ET relationship gained at the catchment scale is transferable to the site scale. If so, it is possible that such an understanding is also applicable at the global scale. Note that site scale refers to the scale at which individual monitoring stations are located. Catchment scale, on the other hand, refers to the scale at which a larger area is studied as a single hydrological system.

To advance the three objectives discussed above, three specific scientific questions are used to guide our analysis at the catchment and site scales using observations to address: 1) Is the GPP-ET linear relationship valid at the catchment scale? 2) If so, can we establish quantitative

linkages between environmental factors and the slope and intercept of this linear relationship at the catchment scale? 3) How are the new quantitative understandings transferable from the catchment scale to the site and regional scales? The rest of this paper is organized as follows: Section 2 introduces the data. Section 3 describes the methods. Section 4 presents the results. Section 5 summarizes the conclusions.

## 2. Data

We use the catchment-scale data directly from the Catchment Attributes and Meteorology for Large-Sample Studies (CAMELS) dataset (Addor et al., 2017; Newman et al., 2015). CAMELS provides daily hydrometeorological observations, such as precipitation, vapor pressure, shortwave radiation, minimum air temperature, maximum air temperature, and streamflow, for over three decades (1982 to 2014). It also includes daily ET simulations in the same period from the integrated Snow-17/SAC-SMA model (Addor et al., 2017; Burnash, 1995). Static catchment attributes, including dominant vegetation type (and its areal fraction in a catchment) and Green Vegetation Fraction (GVF) difference, are also available from CAMELS. GVF represents the fraction of a catchment area covered by green vegetation. The green and non-green portions are assumed to be areas that do or do not transpire, respectively. GVF difference is the difference between the maximum and minimum monthly mean GVF. It represents the seasonal dynamics in the catchment area contributing to the water balance through transpiration.

We also use the GPP data retrieved from Landsat GPP products over the contiguous United States (CONUS) with a spatial resolution of 30-meter and a temporal resolution of 16-day (Robinson et al., 2018). We choose Landsat GPP over the other satellite-based products because it has a 36-year observational period (1991-2021), which overlaps with the CAMELS dataset for 29 years.

Figure 2 summarizes the data used in this study. Harmonization and processing of the data from various sources are detailed in the following seven steps:

1) The CAMELS dataset provides an integrated Snow-17/SAC-SMA model output for ten optimal parameter sets. We collect the daily ET produced with each parameter set and compute the daily ensemble mean ($ET_{ensemble}$).
2) The annual ensemble mean ET ($\overline{\mathrm{ET}}_{\mathrm{ensemble}}$) is then validated against the observed annual mean ET ($\overline{\mathrm{ET}}_{\mathrm{obs}}$). $\overline{\mathrm{ET}}_{\mathrm{obs}}$ is calculated as annual mean precipitation minus annual mean runoff depth (estimated from the observed streamflow and catchment area). We only keep those CAMELS catchments satisfying $\frac{|\overline{\mathrm{ET}}_{\mathrm{obs}}-\overline{\mathrm{ET}}_{\mathrm{ensemble}}|}{\overline{\mathrm{ET}}_{\mathrm{obs}}} \times 100\% \leq 10\%$ for further analysis.
3) For catchments selected in Step 2, we remap the gridded Landsat GPP to each catchment and then convert the 16-day to monthly time series.
4) We identify 1986-2010 as the study period during which all hydroclimatic variables and Landsat GPP data are continuously available (i.e., no missing data) for most catchments selected in Step 2. After filtering out catchments with missing data, we obtain 392 catchments.
5) We define the dominant vegetation cover for each catchment as the single vegetation type covering at least 50% of the drainage area. Hence, we exclude those catchments that do not have any vegetation type covering no less than 50% of the catchment area. We finally obtained 380 catchments with drainage areas ranging from 6.25 to 25,818 $km^2$ (Fig. 3).
6) For convenience, we classify the 380 catchments into six groups based on their dominant vegetation type, resulting in three forested and three non-forested catchment groups

(Table 1). Forested catchments include Deciduous Broadleaf (DBF) (89), Evergreen Forest (Needle leaf + Broadleaf) (EF) (25), and Mixed Forests (MF) (50) dominated catchments. Non-forested catchments include Croplands plus Croplands/Natural Vegetation Mosaic (CL/NVM) (111), Grasslands (GL) (46), and a combination of Savannas, Woody Savannas, and Open/Closed Shrublands, hereafter WSSL catchments (59).

7) We calculate some climatic variables based on the existing CAMELS data. For instance, Vapor Pressure Deficit (VPD) represents the difference between actual and saturation vapor pressure, which we use to represent the atmospheric water demand of plants. We take the daily actual vapor pressure data directly from CAMELS. We calculate daily saturation vapor pressure as the mean of saturation vapor pressure at maximum and minimum air temperatures with the Magnus formula (Parish & Putnam, 1977). Inputs for the Magnus formula are daily air temperature data from CAMELS.

Figure 3 shows the spatial maps (for the 380 catchments) of dominant vegetation types (Fig. 3a), the ensemble annual mean ET in 1986-2010 (Fig. 3b), and the long-term mean annual GPP in 1986-2010 (Fig. 3c).

In addition to the catchment-scale data, we collect the site-scale monthly data over CONUS, mainly from the AmeriFlux dataset (Pastorello et al., 2020). We select 35 AmeriFlux sites in CONUS, as listed in Table 2, with a minimum of 36 months (not necessarily continuous) of both GPP and ET observations in 1986-2010. Note that the data's starting years, ending years, and lengths vary among the sites. Table 2 provides more details about these sites. We obtain daily forcing data from Daymet (Thornton et al., 2021), including minimum and maximum temperature, actual vapor pressure, shortwave radiation, and snow for the 35 sites. For consistency, we also group these sites into the six classes of vegetation types, which yielded five DBF, four EF (all evergreen needleleaf), five GL, eight WSSL (three open shrublands, three closed shrublands, one savannah, and one woody savannah), and thirteen CL/NVM (twelve CL and one NVM) sites.

# 3. Methods

In this study, we first develop a generic expression of the GPP-ET linear relationship that includes both the slope and intercept at the catchment scale (3.1). Data at the catchment scale described above are used to evaluate the validity of the GPP-ET linear relationship and calibrate the parameters (slope and intercept) of the relationship. Analysis is then performed to understand the spatial variability of the parameter values and to derive a multilinear regression relationship between the parameters and various climatic and environmental factors. The regression relationship is used to regionalize the parameters, and the validity of the regionalization is further tested at the site scale using the site-specific data described above. The statistical analysis techniques used in this study are briefly described in 3.2.

## 3.1. Generic form of GPP- ET relationship at the catchment scale

In catchment hydrology, normalization is a typical strategy to form a generic formula by minimizing the impacts of catchment size or magnitudes of any specific variables (Abeshu & Li, 2021; Chen et al., 2013; Chen & Sivapalan, 2020; Wang & Tang, 2014; Ye et al., 2015). Here we assume that normalized monthly GPP and ET at the catchment scale are linearly related as

$$\frac{\mathrm{GPP_m}}{\overline{\mathrm{GPP}}} = \mathrm{a}\frac{\mathrm{ET_m}}{\overline{\mathrm{ET}}} + \mathrm{b} \quad (2)$$

Where $GPP_m$ and $ET_m$ are monthly GPP (gC/m$^2$/day) and ET (mm/day) at the catchment scale, respectively, and $\overline{\mathrm{GPP}}$ and $\overline{\mathrm{ET}}$ are their corresponding long-term averages. $\boldsymbol{a}$ and $\boldsymbol{b}$ are dimensionless linear coefficients.

Rearranging Eqn. (2) for $GPP_m$, we get

$$\mathrm{GPP_m} = \frac{\overline{\mathrm{GPP}}}{\overline{\mathrm{ET}}}(\mathrm{aET_m} + \mathrm{b}\overline{\mathrm{ET}}). \quad (3)$$

$\frac{\overline{\mathrm{GPP}}}{\overline{\mathrm{ET}}}$ is essentially the long-term mean ecosystem water use efficiency. Eqn. (3) can be simplified as

$$\mathrm{GPP_m} = \beta \mathrm{ET_m} + \alpha\overline{\mathrm{ET}} \quad (4)$$

Where $\beta$ $(gC/m2/mm)$ and $\alpha$ $(gC/m2/mm)$ are two parameters. Eqn. (4) represents a two-parameter linear relationship between GPP and ET that can be used to predict GPP given ET. $\beta$ quantifies the increasing rate of GPP with increasing ET and vice versa, implying vegetation carbon uptake per unit of water use. $\alpha$ is associated with the dormant season when GPP or ET is low. The intercept term (i.e., $\alpha * \overline{\mathrm{ET}}$) is analogous to the residual conductance term employed in plant stomatal conductance models (Medlyn et al., 2011). If $\alpha > 0$, plant carbon uptake persists even when both transpiration and evaporation stop due to low VPD ($ET \approx 0$ and $GPP > 0$). If $\alpha < 0$, evaporation continues to occur when there is no GPP associated with the above-ground biomass ($ET > 0$ and $GPP \approx 0$). If $\alpha \approx 0$, evapotranspiration and carbon uptake approach zero simultaneously ($ET \approx 0$ and $GPP \approx 0$).

Note that if $\alpha = 0$, Eqn. (4) essentially reduces to Eqn. (1). Hereafter, we refer Eqn. (1) to as *function-I* and Eqn. (4) as *function-II* for future comparison. We determine the parameters for *function-I* and *function-II* in two stages. In the first stage, monthly GPP and ET data for each catchment (see Section 2) from 1986 to 2002 were used to calibrate the parameters. We then utilize these calibrated parameters to determine monthly GPP in 2003-2010 and verify them against Landsat GPP. The parameter values obtained in the first stage are denoted as "calibrated". In the second stage, we explore and derive quantitative regression relationships between the calibrated *function-II* parameters and climatic and environmental factors such as precipitation, solar radiation, VPD, geography (i.e., the latitude and longitude at the centroid of each catchment), etc. This way, the *function-II* parameters can be estimated a priori instead of through calibration and are denoted as "estimated". Note that these quantitative regression relationships, if successfully derived, can be used to regionalize the *function-II* parameters and provide parameter estimates over sparsely measured locations (Ali et al., 2014; Beck et al., 2020; Merz & Blöschl, 2004; Ye et al., 2014).

## 3.2. Statistical methods

The seasonal dynamics of meteorology, hydrology, and vegetation play an essential role in understanding the spatial variations of the slope and intercept of the GPP-ET linear relationship. The Seasonality Index (SI), as defined below, is used to quantify the seasonal dynamics of different processes. Various statistical metrics, including Pearson and Spearman's correlation coefficients and Kling-Gupta Efficiency, are used to evaluate the validity of the GPP-ET linear relationship. Principal Component Analysis is used to determine the variance of the parameters of the GPP-ET relationship explained by climatic and environmental factors. Lastly, the Variance Inflation Factor (VIF) is used to determine the multicollinearity between the various

climatic and environmental factors used as predictors in a regression formula to predict the parameters of the GPP-ET relationship. These various statistical methods are briefly explained below.

*Seasonality Index* (SI): SI applies to a time series of any time-varying variable and quantifies its seasonal distribution. SI is computed with the Walsh & Lawler (1981) method. SI ranges between 0 and 1.833, indicating that this variable uniformly occurs over the 12 months in a year and within a single month, respectively.

*Pearson correlation coefficient (Pearson's r)*: *Pearson's r* is a statistical metric used to evaluate the linearity of a relationship between paired data. Its numerical value ranges from -1 to +1, where a perfect positive and negative association is indicated by values of +1 and -1, respectively, while a value of 0 indicates no association. Evans (1996) provides the following interpretation of the absolute values of Pearson's r as: < 0.2 – very weak, 0.2 to 0.4 – Weak, 0.4 to 0.6 – Moderate, 0.6 to 0.8 – Strong, ≥ 0.8–Very strong.

*Spearman's correlation (Spearman's ρ):* Spearman's correlation is a statistical measure that assesses the strength and direction of a monotonic relationship between paired data, whether it is linear or not. The magnitude of the correlation coefficient ranges from -1 to +1, indicating perfect negative and positive monotonic relationships, respectively. The absolute value of Spearman's ρ is often interpreted using the following rule of thumb: 0 to 0.20 – negligible, 0.21 to 0.40 – weak, 0.41 to 0.60 – moderate, 0.61 to 0.80 – strong, and 0.81 to 1.00 – very strong.

*Kling-Gupta Efficiency (KGE)*: We use KGE (Kling et al., 2012) as the goodness-of-fit measure for calibrating and validating *function-I* and *function-II*. The KGE value ranges between $-\infty \; to \; 1$. KGE = 1 implies a perfect agreement between observed and simulated data.

*Principal Component Analysis (PCA)*: we use PCA to measure how much variability of parameters, $\beta$ and $\alpha$, can be explained by the catchment climatic and geographic variables.

*Variance Inflation Factor (VIF)*: Multicollinearity between components of any regression formula is tested using the VIF method (Miles, 2014; Neter et al., 1983). Generally, if 5.0 < VIF < 10.0, the multicollinearity issue requires further investigation. VIF >10 is a sign of severe multicollinearity and must be corrected. Remedial measures are necessary until VIF is less than 5.0 between any two components. A typical remedial strategy is to use more tolerant regression techniques such as the least absolute shrinkage and selection operator (LASSO) and Ridge regression (Dormann et al., 2013; Franke, 2010).

# 4. Results

## 4.1. Validating the GPP-ET linear relationship at the catchment scale

Linearity analysis via *Pearson's r* suggests that the catchment-scale GPP-ET linear relationship is indeed valid regardless of catchment size, climate, topography, or vegetation type (Fig. 4). *Pearson's r* in 1986-2010 is higher than 0.6 for 97% of the 380 catchments, and is higher than 0.8 for 88% of them. Only 12 (3%) catchments have *Pearson's r* lower than 0.6. These 12 catchments are all located in an arid climate, and WSSL dominates 9 of them. The relatively low *Pearson's r* values in the arid catchments are likely due to two reasons: i) the uncertainty in ET estimation from the SAC-SMA model (Newman et al., 2015) and ii) the increase in the relative importance of evaporation components besides transpiration. Note that, even among these 3% catchments, *Pearson's r* is still no less than 0.4 except for two catchments, indicating a certain level of linearity.

Fig. 4 also shows the scatter plots of monthly GPP versus ET normalized by their corresponding long-term mean in 1986-2010 for 16 representative catchments (Fig. 4a-p). The 16 catchments are selected in two steps. First, the 380 catchments are divided into three geographic groups based on longitude: the eastern, western, and central US regions. Then six catchments from the eastern, five from the central, and five from the western US are selected based on the strength of GPP seasonality, i.e., SI values ranging from the minimum to the maximum. Clearly, the intercept is not negligible for some catchments and varies even among the same vegetation types.

Indeed, *function-II* performs better than *function-I* in those catchments dominated by grasslands and shrubs, as suggested by Fig. 5. In this study, we calibrate the parameters for both *function-I* and *function-II* in the calibration period 1986-2003 and use the calibrated parameters to predict the monthly GPP in the validation period 2003-2010. Fig. 5 displays the monthly KGE values (between the predicted and observed GPP time series) for all 380 catchments (map in the middle) in 2003-2010. It also shows the predicted and observed monthly GPP time series for the 16 representative catchments (Fig. 5a-p). For those catchments dominated by grasslands and shrubs (Fig. 5b, c, d, g, and m), *function-I* is subject to at least noticeable overestimation in June-August when GPP is highest and underestimation in November-January when GPP is lowest. However, *function-II* eliminates these noticeable biases. Fig. 5q summarizes this comparison between *function-I* and *function-II* in terms of Cumulative Distribution Function (CDF) for the KGE values (between the observed and predicted monthly GPP) in the calibration and validation periods, respectively. A CDF curve here describes the percentage of the 380 catchments with their KGE values below a certain threshold. For example, CDF at KGE = 0.8 indicates the percentage of the 380 catchments with KGE ≤ 0.8. *Function-II* achieves KGE ≥ 0.8 for 333 of the 380 catchments, whilst *function-I* achieves KGE ≥ 0.8 for only 158 catchments. Over the CONUS domain, *function-II* performs better by better capturing both the maximum and minimum of the GPP values, hence better capturing the seasonality of the GPP time series.

The calibrated slope, $\beta$, values from *function-II* are larger than those calibrated $\omega$ values from *function-I* (i.e., the ratio of long-term mean GPP to long-term mean ET) values at ~70.5% of the 380 catchments suggesting that the insights on the slope of the GPP-ET relationship gained from previous site-scale studies may not be directly applicable to the catchment and larger scales. Moreover, the absolute values of the calibrated intercept, $\alpha * \overline{\mathrm{ET}}$, are nonzero (i.e., >0.05gC/m$^2$/day) for 96% of the 380 catchments. This indicates that, in part, including the intercept in the linear equation is responsible for the calibrated slope being consistently greater than the traditional ones in a large proportion of the catchments. Hence, the previous understanding of the GPP-ET relationship needs to be reexamined at the catchment scale via the lens of *function-II* and its parameters.

## 4.2. Understanding the *function-II* parameters

The spatial patterns of the calibrated $\beta$ and $\alpha$ values (Fig. 6) are similar to that of the annual mean GPP (Fig. 3). Roughly, $\beta$ decreases from northeast to southwest, except for catchments along the Pacific Northwest coast. Physically, $\beta$ represents the vegetation carbon uptake per millimeter of water. At a given geographic longitude, $\beta$ and $\alpha$ increase and decrease with latitude, respectively. Their spatial patterns are closely related to the climate and environmental factors of CONUS that vary with latitude. Generally, mean annual vapor pressure deficit and solar radiation decrease northward, and precipitation seasonality is strong in the central and western US and weak in the eastern US and the Rocky Mountains. Furthermore, the phase index between PET and precipitation is moderately negatively correlated with $\alpha$ ($Spearman's\ \rho$ = -0.40) but exhibits no significant association with $\beta$. On the other hand, the parameter $\beta$ is

negatively correlated with the aridity index (*Spearman's* $\rho$ = -0.65), which is only moderately and positively associated with $\alpha$ (*Spearman's* $\rho$ = 0.436). Both parameters are also significantly associated with precipitation frequency (*Spearman's* $\rho$ = 0.7 for $\beta$ and -0.565 for $\alpha$). The spatial variability of $\beta$ and $\alpha$ also shows strong agreement with the peak mean monthly GVF values ($Spearman's\ \rho$ is 0.75 for $\beta$ and -0.9 for $\alpha$).

The systematic difference in these parameters in catchments with different dominant vegetation types is further shown in Fig. 7. The catchment vegetation phenological cycle imposes significant control on the GPP-ET relationship. In Fig. 7a, from top to bottom, the mean calibrated $\beta$ values (averaged across the catchments) are largest in the DBF-dominated catchments, followed by MF, EF, WSSL, and GL. The large values of $\beta$ in DBF-dominated catchments can be attributed to their markedly distinct phenological stages, including leaf regeneration and senescence, resulting in a rapid shift in carbon uptake between the transient and dormant states. Photosynthesis rarely occurs during the dormant state, even when ET persists due to soil evaporation. The high values of $\beta$ reflect the combined effect of DBF characteristics and environmental factors resulting in a strong GPP seasonality. EF maintains foliage year-round, and even during the dormant season, carbon uptake is higher than other vegetation types, which increases further with greening-up. The phenological characteristics of the EF and the dominant effect of PET result in a relatively subdued GPP seasonality compared to DBF, hence, lower $\beta$ values in comparison. MF is a mixture of DBF and EF, so its calibrated $\beta$ values reasonably lie between those of the two, reflecting a property that emerged from the combined characteristics of EF and DBF forests. In GL catchments, gross primary productivity is primarily driven by temperature and precipitation (both magnitude and timing) and hence, highly dynamic and varies on a days-to-weeks scale. In these catchments, ET is often close to total water availability (Abeshu & Li, 2021). These factors result in very similar monthly variations in ET and GPP, as indicated by the $\beta$ value only slightly greater than one. The WSSL vegetation is combined herbaceous and forested; as such, their calibrated $\beta$ values lie reasonably between those of forested and grassland catchments. For the last vegetation group, i.e., CL/NVM, the phenological stages include temporary crop cover, harvest, and a bare soil period. The phenology and climate characteristics are similar to that of DBF, but human factors also influence this group through fertilization and other management practices that promote crop growth and harvest. The similarity between CL/NVM and DBF explains why the CL/NVM covers have the second-highest calibrated $\beta$ value (on average) after DBF.

The calibrated $\alpha$ values are non-negligible ($|\alpha| > 0.05\ gC/m2/day$) for 360 of the 380 catchments and exhibit systematic differences among the vegetation types. Fig. 7b suggests that positive $\alpha$ values primarily exist in the catchments dominated by WSSL (51 of 59 catchments), EF (17 of 25 catchments), and some GL (16 of 46 catchments). The positive $\alpha$ values suggest a condition under which plant continues to take up carbon, but ET diminishes during the dormant season. For instance, low VPD (high humidity) translates to low transpiration and soil evaporation. However, plant carbon uptake can persist, driven by the energy from solar radiation. Negative $\alpha$ values prevail in the catchments dominated by DBF, MF, GL, and CL/NVM, indicating that soil evaporation takes over during the dormant season when photosynthesis diminishes via phenological processes (DBF, MF, and GL) or human activities (CL/NVM). GPP happens only in the presence of light, but given sufficient VPD, ET occurs all the time; as such, the absence of light can result in a scenario where ET > 0 while GPP = 0. A similar scenario can also manifest under the condition where daytime processes are diminished (i.e., GPP and daytime ET are zero), but night-time ET is not, as daytime and night-time ET respond differently

to low VPD levels (Han & Wang, 2021). Catchments with $\alpha > 0$ are located in the coastal areas of the Pacific Northwest, Pacific Coast, Southwest, Gulf Coast, and the southern part of the Great Plains (for GL) (see Fig. 3a and Fig. 6b). Particularly in the southwestern coastal areas, the winter period atmospheric river precipitation strongly influences the NDVI (Albano et al., 2017). Hence, to a certain degree, this also contributes to $\alpha$ being relatively larger and positive in that area. The winter temperature is relatively mild in these regions of CONUS (Lute & Luce, 2017). The winter temperature decreases systematically from the coastal regions inland, where the rest of the catchments are located. The magnitude of $\alpha$, in general, can be attributed to plant functionality and winter temperature. Plants have a minimum threshold for freezing temperature, beyond which plant radiation conversion efficiency diminishes to zero, hence no photosynthetic activities (i.e., $GPP = 0$). However, driven by solar radiation, soil, and canopy surface evaporation may persist, leading to $ET > 0$ even when transpiration is nonexistent, resulting in $\alpha < 0$. Further, during the winter days, the daytime process, including GPP and ET, might be inhibited by the absence of sufficient photoperiods, but night-time ET can still occur. The $\alpha$ values are particularly greater than zero in the western U.S.

Fig. 7a and b show systematic agreement between the variations of $\beta$ and $\alpha$ with vegetation types, indicating that catchments with strong seasonal variations in GVF have larger $\beta$ values and smaller $\alpha$ values (e.g., DBF) and vice versa (e.g., WSSL). The above differences in the *function-II* parameters among the vegetation regimes can be further explained by the GVF difference (Fig. 7c). GVF difference at the catchment scale quantifies the seasonal changes in the spatial coverage of active greenness within a catchment. For forested catchments, GVF generally decreases from DBF to MF to EF. Both $\beta$ and $\alpha$ show a systematic pattern, with $\beta$ showing a pattern similar to GVF and $\alpha$ opposite to GVF. DBF has thick canopies at the peak of the growing period and loses most leaves in winter, resulting in relatively large temporal dynamics of spatial cover (GVF difference$> 0.4$). EF catchments, on the other hand, maintain most of the canopy cover year-round (GVF difference$< 0.2$). The MF type, as expected, lies between the two, reflecting the influence of both vegetation types. From Fig. 7c, one can see that GL catchments have a wide range of GVF values, implying that some catchments are dominated by perennial grasslands with low GVF differences, while others are seasonal grasslands with higher GVF differences. The GVF difference is generally low in the WSSL catchments (<0.2) because this category is a mixture of forest and grasslands (perennial or seasonal), and the green canopy coverage remains relatively stable throughout the year. To generalize, catchments with rapid seasonal change in spatial cover are characterized by relatively high positive slope and high negative intercept in the GPP-ET linear relationship, while catchments with subdued seasonal dynamics are characterized by relatively smaller slope and smaller but positive intercept in the GPP-ET relationship. To a certain degree, these characteristics indicate a space-time similarity of catchment vegetation dynamics.

## 4.3. Regionalizing the *function-II* parameters

Taking advantage of the insights gained from the above analyses, we attempt to regionalize the *function-II* parameters by estimating the function-II parameters a priori at the regional scale. Parameter regionalization is an effective strategy to transfer the process-based understanding from gaged to ungaged catchments and from catchment- to regional scale (Abeshu & Li, 2021; Guo et al., 2014; Ye et al., 2014). We aim to identify regression relationships between the target variables ($\beta$ and $\alpha$ in this case) and climate and other environmental factors as predictors. We do not explicitly include phenological variables, such as GVF, as predictors primarily because the

447 phenological characteristics of vegetation are already closely related to climate and
448 environmental conditions.

449 The environmental factors for consideration are mostly static, such as geographic locations, soil
450 properties, geography, etc. The climatic factors are expressed in terms of seasonality index,
451 mean, maximum, or minimum values extracted from the corresponding time series in 1986-2010.
452 Here we select the climate and environmental predictor variables based on two criteria: 1)
453 observational data of these factors should be extensively available globally; 2) the factors should
454 have good monotonic relationships with $\beta$ and $\alpha$, at least for some vegetation types. After a few
455 rounds of trial and error, we identify the following predictor variables that satisfy the two criteria
456 and lead to the best possible regression formulas: Geographic latitude (*Lat*), Long-term mean
457 VPD ($\overline{VPD}$), Minimum monthly mean VPD ($VPD_{min}$), Long-term mean shortwave radiation
458 ($\overline{SWR}$), Minimum monthly mean SWR ($SWR_{min}$), Long-term mean snow fraction ($\overline{SF}$), and the
459 Seasonality index of monthly precipitation ($SI_p$).

460 We use Spearman's ρ to determine whether the above predictors have monotonic relationships
461 with $\beta$ and $\alpha$ for each vegetation type, as shown in Fig. 8. For instance, latitude has moderate to
462 strong monotonic relationships with both $\beta$ and $\alpha$ (|*Spearman's* $\rho$| > 0.4) among most vegetation
463 regimes, except for WSSL. $\overline{SWR}$ has strong monotonic relationships with both $\beta$ and $\alpha$
464 (|*Spearman's* $\rho$| > 0.6) in catchments dominated by DBF, MF, GL, CL/NVM. Furthermore, we
465 perform principal-component-analysis (PCA) to assess if the predictors included in Fig. 8
466 explain the most variability in the *function-II* parameters, as shown in Fig. 9. It appears that the
467 first two PCA components alone can explain more than 80% of the variability of both $\beta$ and $\alpha$
468 within each vegetation regime, suggesting that these climatic and environmental factors can
469 potentially well predict both $\beta$ and $\alpha$ for each vegetation regime at the catchment scale.

470 We obtain two multilinear regression formulas for $\beta$ and $\alpha$, separately.

$$\beta = 1.615 - 0.0056(ln(\overline{SWR}) * Lat) - 2.087\ ln\ ln\ (\overline{VPD}) - 1.081(\overline{SF} * SI_P) \quad (5)$$

$$\alpha = 7.956 + 1.958\ (ln\ ln\ VPD_{min} * Lat) + 1.369(SI_P + \overline{SF})\ - 1.364SWR_{min} \quad (6)$$

471 It is possible that multicollinearity exists among the predictors. Hence, we check for
472 multicollinearity using VIF. The VIF is $< 2.75$ for $\beta$, and $< 5.50$ for $\alpha$, indicating that the
473 regression formulas (Eqn. 5 and 6) are reasonably free from multicollinearity (Fig. 9).

474 Fig. 10 shows that the regression formulas well capture the spatial variability of $\beta$ and $\alpha$ . KGE
475 and $r^2$ are 0.71 and 0.73 for $\beta$, and 0.81 and 0.79 for $\alpha$, respectively. Between the two
476 parameters, $\alpha$ generally shows a lower difference between the estimated and predicted values.
477 About 72% of catchments for $\beta$ and 78% for $\alpha$ are within a 20% margin of error (i.e., absolute
478 difference divided by actual value). Thirty-nine (~10% of 380: 13 WSSL, 12 EF, 12 GL, and 2
479 CL/NVM) catchments show a deviation larger than 20% for both parameters. We further apply
480 the estimated β and α values in *function-II* against Landsat GPP shows KGE ≥ 0.5 and ≥ 0.80 for
481 92% and 62% of the catchments, respectively (Fig. 11). Only 30 of the 380 catchments have
482 KGE below 0.5, and only three have KGE less than zero. The dominant vegetation types in these
483 30 catchments are GL (15), EF (7), and WSSL (7). The two regression formulas can thus
484 reasonably well regionalize the *function-II* parameters, enabling the transferability of *function-II*
485 over the whole contiguous U.S.

## 4.4. Verifying *function-II* at the Site-scale

Lastly, we evaluate whether *function-II* (Eqn. 4) and its parameter regionalization (Eqn. 5 and 6) at the catchment scale are transferable to the site scale. We compare the simulated GPP (using the site-scale climate and other data described in Section 2) against the AmeriFlux GPP observations at 35 sites and the monthly scale. The results show that *function-II* captures the site-scale GPP reasonably well, as indicated by $R^2 \geq 0.5$ for 32 sites and KGE $\geq 0.5$ for 25 sites (Table 3). The mean and median KGE across all sites are 0.51 and 0.61, respectively. The few sites with relatively poor performances are mainly located in the western U.S., where Eqn. 5 performs relatively poorly even at the catchment scale.

Figure 12 depicts the monthly time series of simulated and observed GPP at five sites, one for each vegetation type. The model captures the reference data well for the DBF site but underestimates the peak values (Fig. 12a). The function consistently overestimates for the EF site (Fig. 12b). Given that the intercept coefficients of both sites are < 0 and the seasonal patterns are reasonably captured (Table 3), the overestimation is mainly due to underestimated intercept (i.e., underestimated $\alpha$), underestimated long-term ET, or both. For WSSL and GL (Fig. 12c and d), the model captures the reference data reasonably well. Similar to the DBF site, the CL/NVM results show poor performance in terms of magnitude but capture the patterns well (Fig. 12e). Further, in general, the poor performances could be attributed to parameter estimation uncertainties. For most of these sites, seeing that the temporal dynamics are captured well in both magnitude and pattern, other than the peak GPP months, the cause is likely a bias in peak period ET (i.e., underestimation) or decoupling between ET and GPP (i.e., linearity does not apply) during this period. Overall, *function-II* provides reasonable estimates of GPP at the site scale, with only three sites having KGE less than zero. Hence our results suggest that *function-II* works across a wide range of spatial scales, given that the study catchments also span a wide range of sizes.

# 5. Discussions

In this study, two GPP-ET formulas at monthly scales are evaluated at the catchment scale: the traditional one-parameter relationship (*function-I*) and the newly proposed two-parameter relationship (*function-II*). Typically, the slope of a GPP-ET relationship is considered as the long-term ecosystem water use efficiency (WUE), which reflects climatic and phenological controls on vegetation carbon gain and water consumption. The superior performance of *function-II* suggests that the *function-II* slope, β, is a more reliable estimator of WUE than the *function-I* slope, ω. Fig. 13 shows that β significantly differs from ω in most catchments, particularly for cases where ω was larger than $2gC/m^2/mm$. Compared to β, ω overestimates WUE in the southwestern catchments dominated by EF and WSSL, where seasonality of GPP is weak, and underestimates it in those northeastern catchments dominated by DBF, MF, GL, and CL/NVM, where seasonality of GPP is strong.

WUE is a widely employed indicator for evaluating an ecosystem's adaptability to changing environmental conditions. An overestimation of WUE may create the impression that ecosystems are more resilient to water stress than they truly are, impacting our understanding of their adaptability to climate change (J. Huang et al., 2016). Furthermore, such overestimation can misrepresent an ecosystem's contribution to carbon sequestration, implying it can assimilate more carbon dioxide per unit of water consumed than it actually can (Keenan et al., 2013). Furthermore, fluctuations in WUE under extreme circumstances can trigger cascading effects on ecosystem functioning. For instance, overestimating WUE may lead to a false sense of ecosystem resilience to drought, whereas underestimation could result in overlooking the potential repercussions of drought or other water stresses on ecosystems (Leuzinger et al., 2011). Such misjudgments can prompt improper management decisions and produce adverse ecological consequences. An underestimation of WUE may lead to similar misjudgments as above except in an opposite direction, e.g., overestimation of ecosystem resiliency under water stress. Reliable estimation of WUE across diverse plant species and ecosystems is crucial for biodiversity conservation, as it helps identify species and ecosystems more susceptible to climate change (Chaves et al., 2003). Such knowledge can inform targeted conservation efforts to safeguard vulnerable species and habitats.

Despite the improved performance of *function-II* (over *function-I)*, certain limitations persist. Firstly, the GPP-ET linearity is weaker in some catchments than the rest due to noticeable contribution from surface evaporation. Hence the proposed function could be further improved in such areas. Secondly, the proposed function does not capture monthly peak GPP values in some cases. The likely reasons include: biases in ET estimation, WUE may vary from one season to another (or vary at a longer time scale) instead of being constant. Both are beyond the scope of this study and left for future work. Lastly, ET is used as a whole instead of partitioning explicitly into transpiration and evaporation. ET partitioning is a long-standing challenge in both ecologic and hydrologic communities. These limitations, nevertheless, do not affect our conclusions, but rather open new opportunities for future research.

# 6. Conclusions

This study presents a generalized monthly GPP-ET relationship that works well across the catchment and site scales, hence regional scale as well. Driven by three objectives and the corresponding scientific questions, we have analyzed data at 380 catchments across CONUS. For the question "*Is the GPP-ET linear relationship valid at the catchment scale*", we find a strong linear relationship between monthly GPP and ET for most catchments (*Pearson's r* > 0.6 for 97%

of the 380 catchments) except for a few arid catchments dominated by woody savanna or shrublands. We also find a non-negligible linear intercept of the GPP-ET relationship at the catchment scale for 360 catchments. Hence, we argue that a new, generalized GPP-ET relationship with a non-zero intercept is more suitable at the catchment and monthly time scale. For the question "*Can we establish quantitative linkages between environmental factors and the slope and intercept of this linear relationship at the catchment scale*", we have established quantitative linkages between the parameters of the new GPP-ET relationship and the climatic and environmental factors. We have also developed and validated a parameter regionalization strategy (based on multilinear regression analysis), enabling the transferability of the new GPP-ET relationship from gaged to ungauged catchments. For the question "*How is the new quantitative understanding transferable from the catchment scale to the site and regional scales*", we have verified the new GPP-ET relationship and its parameter regionalization at 35 AmeriFlux sites with relatively satisfactory performance. We attribute the seemingly higher biases at the site scale (compared to the catchment scale) to the difference in the input data sources and the uncertainty in the parameter regionalization. Taken together, we suggest that the new GPP-ET relationship and its parameter regionalization can be transferable across the site, catchment, and regional scales.

The outcomes from this study have at least three important implications: 1) They can bridge the ecological and hydrologic communities by providing a unified understanding of ET (water cycle) and its linkages to vegetation productivity (carbon cycle). Any future new understanding of GPP from the ecologic community and water balance from the hydrologic community can likely further advance our understanding of this generalized GPP-ET relationship, coupling between the water and carbon cycles, and other individual ecological and hydrologic processes. 2) They can be used as physically meaningful indicators of the coupled hydrological-ecological processes to diagnose the simulation results from land surface and earth system models. Such diagnosis will shed light on the possible deficiencies in these models' structures or parameterizations for representing hydrological and ecological processes and their interactions. 3) They can be used to provide physical constraints for remote sensing-based ET products. Such products have been subject to substantial biases, particularly during cloudy days. Remote-sensing measurements provide valuable GPP and ET products at various spatiotemporal resolutions, but almost all of these products are obtained from optical spectral measurements, which clouds can easily contaminate. This can lead to uncertainty in the measurement quality of each revisit at a certain location, especially for regions with persistent cloud cover throughout the year, such as the Amazon (Samanta et al., 2012; Xu et al., 2019). This research provides a foundation for recompiling GPP and ET products from multiple instruments with varying resolutions. Given the GPP-ET relationships shown in this paper, it is extraordinarily meaningful to apply the GPP-ET relationships obtained from different ecosystems to multiple satellite products, which could reduce uncertainties and reproduce data products with enhanced spatial and temporal coverage.

## Acknowledgments

This research was supported as part of the Energy Exascale Earth System Model (E3SM) project, funded by the US Department of Energy, Office of Science, Office of Biological and Environmental Research as part of the Earth System Model Development program area. G. Abeshu and H.-Y. Li were also supported by the US National Science Foundation (EAR #1804560). M. Shi was partly supported by the US Department of Energy Office of Science Biological and Environmental Research as part of the Terrestrial Ecosystem Science Program through the Next-Generation Ecosystem Experiments (NGEE) Tropics project. N. McDowell was supported by the US Department of Energy, Office of Science, Office of Biological and Environmental Research through the River Corridor Scientific Focus Area at Pacific Northwest National Laboratory. The Pacific Northwest National Laboratory is operated by Battelle for the US Department of Energy under Contract DE-AC05-76RL01830.

# References


Abeshu, G. W., & Li, H. Y. (2021). Horton Index: Conceptual Framework for Exploring Multi-Scale Links Between Catchment Water Balance and Vegetation Dynamics. *Water Resources Research*, *57*(5), 1–24. https://doi.org/10.1029/2020WR029343

Addor, N., Newman, A. J., Mizukami, N., & Clark, M. P. (2017). The CAMELS data set: Catchment attributes and meteorology for large-sample studies. *Hydrology and Earth System Sciences*, *21*(10), 5293–5313. https://doi.org/10.5194/hess-21-5293-2017

Albano, C. M., Dettinger, M. D., & Soulard, C. E. (2017). Influence of atmospheric rivers on vegetation productivity and fire patterns in the southwestern U.S. *Journal of Geophysical Research: Biogeosciences*, *122*(2), 308–323. https://doi.org/10.1002/2016JG003608

Ali, M., Ye, S., Li, H. yi, Huang, M., Leung, L. R., Fiori, A., & Sivapalan, M. (2014). Regionalization of subsurface stormflow parameters of hydrologic models: Up-scaling from physically based numerical simulations at hillslope scale. *Journal of Hydrology*, *519*(PA), 683–698. https://doi.org/10.1016/j.jhydrol.2014.07.018

Bacon, M. (2004). *Water Use Efficiency in Plant Biology*.

Baldocchi, D. (1994). A comparative study of mass and energy exchange rates over a closed C3(wheat) and an open C4(corn) crop: II. CO2 exchange and water use efficiency. *Agricultural and Forest Meteorology*, *67*(3), 291–321.

Baldocchi, D., & Ryu, Y. (2011). Forest Hydrology and Biogeochemistry. In D. F. Levia, D. Carlyle-Moses, & T. Tanaka (Eds.), *Forest hydrology and biogeochemistry, Synthesis of past research and future directions* (Vol. 216). Dordrecht: Springer Netherlands. https://doi.org/10.1007/978-94-007-1363-5

Baldocchi, D., Falge, E., Gu, L., Olson, R., Hollinger, D., Running, S., et al. (2001). FLUXNET: A New Tool to Study the Temporal and Spatial Variability of Ecosystem-Scale Carbon Dioxide, Water Vapor, and Energy Flux Densities. *Bulletin of the American Meteorological Society*, *82*(11), 2415–2434. https://doi.org/10.1175/1520-0477(2001)082<2415:FANTTS>2.3.CO;2

Beck, H. E., Pan, M., Lin, P., Seibert, J., van Dijk, A. I. J. M., & Wood, E. F. (2020). Global Fully Distributed Parameter Regionalization Based on Observed Streamflow From 4,229 Headwater Catchments. *Journal of Geophysical Research: Atmospheres*, *125*(17). https://doi.org/10.1029/2019JD031485

Beer, C., Reichstein, M., Ciais, P., Farquhar, G. D., & Papale, D. (2007). Mean annual GPP of Europe derived from its water balance. *Geophysical Research Letters*, *34*(5), 13–16. https://doi.org/10.1029/2006GL029006

Beer, C., Ciais, P., Reichstein, M., Baldocchi, D., Law, B. E., Papale, D., et al. (2009). Temporal and among-site variability of inherent water use efficiency at the ecosystem level. *Global Biogeochemical Cycles*, *23*(2). https://doi.org/10.1029/2008GB003233

Beer, C., Reichstein, M., Tomelleri, E., Ciais, P., Jung, M., Carvalhais, N., et al. (2010). Terrestrial gross carbon dioxide uptake: Global distribution and covariation with climate. *Science*, *329*(5993), 834–838. https://doi.org/10.1126/science.1184984

Boese, S., Jung, M., Carvalhais, N., & Reichstein, M. (2017). The importance of radiation for semiempirical water-use efficiency models. *Biogeosciences*, *14*(12), 3015–3026. https://doi.org/10.5194/bg-14-3015-2017

Bonan, G. B., Patton, E. G., Harman, I. N., Oleson, K. W., Finnigan, J. J., Lu, Y., & Burakowski, E. A. (2018). Modeling canopy-induced turbulence in the Earth system: A unified parameterization of turbulent exchange within plant canopies and the roughness sublayer (CLM-ml v0). *Geoscientific Model Development*, *11*(4), 1467–1496.

https://doi.org/10.5194/gmd-11-1467-2018

Brooks, P. D., Troch, P. A., Durcik, M., Gallo, E., & Schlegel, M. (2011). Quantifying regional scale ecosystem response to changes in precipitation: Not all rain is created equal. *Water Resources Research*, *47*(7), 1–13. https://doi.org/10.1029/2010WR009762

Brümmer, C., Black, T. A., Jassal, R. S., Grant, N. J., Spittlehouse, D. L., Chen, B., et al. (2012). How climate and vegetation type influence evapotranspiration and water use efficiency in Canadian forest, peatland and grassland ecosystems. *Agricultural and Forest Meteorology*, *153*, 14–30. https://doi.org/10.1016/j.agrformet.2011.04.008

Budyko, M. I. (1974). *Man and Climate*. *Climate and Life*. Academic Press.

Burnash, R. (1995). The NWS River Forecast System-Catchment Modeling. In V. Singh (Ed.), *Computer Models of Watershed Hydrology* (pp. 311–366). Colorado: Water Resources Publication.

Chaves, M. M., Maroco, J. P., & Pereira, J. S. (2003). Understanding plant responses to drought - From genes to the whole plant. *Functional Plant Biology*, *30*(3), 239–264. https://doi.org/10.1071/FP02076

Chen, X., & Sivapalan, M. (2020). Hydrological Basis of the Budyko Curve: Data-Guided Exploration of the Mediating Role of Soil Moisture. *Water Resources Research*, *56*(10), 1–15. https://doi.org/10.1029/2020WR028221

Chen, X., Alimohammadi, N., & Wang, D. (2013). Modeling interannual variability of seasonal evaporation and storage change based on the extended Budyko framework. *Water Resources Research*, *49*(9), 6067–6078. https://doi.org/10.1002/wrcr.20493

Choudhury, B. J. (1999). Evaluation of an empirical equation for annual evaporation using field observations and results from a biophysical model. *Journal of Hydrology*, *216*(1–2), 99–110. https://doi.org/10.1016/S0022-1694(98)00293-5

Donohue, R. J., Roderick, M. L., & McVicar, T. R. (2007). On the importance of including vegetation dynamics in Budyko's hydrological model. *Hydrology and Earth System Sciences*, *11*(2), 983–995. https://doi.org/10.5194/hess-11-983-2007

Donohue, R. J., Roderick, M. L., & McVicar, T. R. (2010). Can dynamic vegetation information improve the accuracy of Budyko's hydrological model? *Journal of Hydrology*, *390*(1–2), 23–34. https://doi.org/10.1016/j.jhydrol.2010.06.025

Dormann, C. F., Elith, J., Bacher, S., Buchmann, C., Carl, G., Carré, G., et al. (2013). Collinearity: A review of methods to deal with it and a simulation study evaluating their performance. *Ecography*, *36*(1), 27–46. https://doi.org/10.1111/j.1600-0587.2012.07348.x

Evans, J. D. (1996). *Straightforward statistics for the behavioral sciences*. Pacific Grove, CA: Thomson Brooks/Cole Publishing.

Farquhar, G. D., Ehleringer, J. R., & Hubick, K. T. (1989). Carbon Isotope Discrimination and Photosynthesis. *Annual Review of Plant Physiology and Plant Molecular Biology*, *40*(1), 503–537. https://doi.org/10.1146/annurev.pp.40.060189.002443

Franke, G. R. (2010). Multicollinearity. In *Wiley International Encyclopedia of Marketing*. John Wiley & Sons, Ltd. https://doi.org/https://doi.org/10.1002/9781444316568.wiem02066

Fu, B. (1981). On the calculation of the evaporation from land surface. *Chinese Journal of Atmospheric Sciences*, *5*(1), 23–31. https://doi.org/10.3878/j.issn.1006-9895.1981.01.03

Gentine, P., Green, J. K., Guérin, M., Humphrey, V., Seneviratne, S. I., Zhang, Y., & Zhou, S. (2019). Coupling between the terrestrial carbon and water cycles - A review. *Environmental Research Letters*, *14*(8). https://doi.org/10.1088/1748-9326/ab22d6

Greve, P., Gudmundsson, L., Orlowsky, B., & Seneviratne, S. I. (2015). Introducing a probabilistic Budyko framework. *Geophysical Research Letters*, *42*(7), 2261–2269. https://doi.org/10.1002/2015GL063449

Greve, P., Gudmundsson, L., Orlowsky, B., & Seneviratne, S. I. (2016). A two-parameter Budyko function to represent conditions under which evapotranspiration exceeds precipitation. *Hydrology and Earth System Sciences*, *20*(6), 2195–2205. https://doi.org/10.5194/hess-20-2195-2016

Guo, J., Li, H. Y., Leung, L. R., Guo, S., Liu, P., & Sivapalan, M. (2014). Links between flood frequency and annual water balance behaviors: A basis for similarity and regionalization. *Water Resources Research*, *50*(2), 937–953. https://doi.org/10.1002/2013WR014374

Han, Q., & Wang, T. (2021). Comparison of Nighttime With Daytime Evapotranspiration Responses to Environmental Controls Across Temporal Scales Along a Climate Gradient Water Resources Research, 1–18. https://doi.org/10.1029/2021WR029638

Hatfield, J. L., & Dold, C. (2019). Water-use efficiency: Advances and challenges in a changing climate. *Frontiers in Plant Science*, *10*(February), 1–14. https://doi.org/10.3389/fpls.2019.00103

Horton, R. E. (1933). The Role of infiltration in the hydrologic cycle. *Eos, Transactions American Geophysical Union*, *14*(1), 446–460. https://doi.org/10.1029/TR014i001p00446

Huang, J., Yu, H., Guan, X., Wang, G., & Guo, R. (2016). Accelerated dryland expansion under climate change. *Nature Climate Change*, *6*(2), 166–171. https://doi.org/10.1038/nclimate2837

Huang, M., Piao, S., Sun, Y., Ciais, P., Cheng, L., Mao, J., et al. (2015). Change in terrestrial ecosystem water-use efficiency over the last three decades. *Global Change Biology*, *21*(6), 2366–2378. https://doi.org/10.1111/gcb.12873

Huang, M., Piao, S., Zeng, Z., Peng, S., Ciais, P., Cheng, L., et al. (2016). Seasonal responses of terrestrial ecosystem water-use efficiency to climate change. *Global Change Biology*, *22*(6), 2165–2177. https://doi.org/10.1111/gcb.13180

Ito, A., & Inatomi, M. (2012). Water-use efficiency of the terrestrial biosphere: A model analysis focusing on interactions between the global carbon and water cycles. *Journal of Hydrometeorology*, *13*(2), 681–694. https://doi.org/10.1175/JHM-D-10-05034.1

Jiang, S., Liang, C., Cui, N., Zhao, L., Liu, C., Feng, Y., et al. (2020). Water use efficiency and its drivers in four typical agroecosystems based on flux tower measurements. *Agricultural and Forest Meteorology*, *295*(September), 108200. https://doi.org/10.1016/j.agrformet.2020.108200

Keenan, T. F., Hollinger, D. Y., Bohrer, G., Dragoni, D., Munger, J. W., Schmid, H. P., & Richardson, A. D. (2013). Increase in forest water-use efficiency as atmospheric carbon dioxide concentrations rise. *Nature*, *499*(7458), 324–327. https://doi.org/10.1038/nature12291

Kling, H., Fuchs, M., & Paulin, M. (2012). Runoff conditions in the upper Danube basin under an ensemble of climate change scenarios. *Journal of Hydrology*, *424–425*, 264–277. https://doi.org/10.1016/j.jhydrol.2012.01.011

Krinner, G., Germany, F., Shongwe, M., Africa, S., France, S. B., Uk, B. B. B. B., et al. (2014). Long-term Climate Change: Projections, Commitments and Irreversibility Pages 1029 to 1076. In *Climate Change 2013 – The Physical Science Basis* (Vol. 9781107057, pp. 1029–1136). Cambridge University Press. https://doi.org/10.1017/CBO9781107415324.024

Kuglitsch, F. G., Reichstein, M., Beer, C., Carrara, A., & Ceulemans, R. (2008). Characterisation of ecosystem water-use efficiency of european forests from eddy covariance measurements. *Biogeosciences Discussions*, *5*(6), 4481–4519. https://doi.org/10.5194/bgd-5-4481-2008

Law, B. E., Falge, E., Gu, L., Baldocchi, D. D., Bakwin, P., Berbigier, P., et al. (2002). Environmental controls over carbon dioxide and water vapor exchange of terrestrial vegetation. *Agricultural and Forest Meteorology*, *113*(1–4), 97–120.

https://doi.org/10.1016/S0168-1923(02)00104-1
Leuzinger, S., Luo, Y., Beier, C., Dieleman, W., Vicca, S., & Körner, C. (2011). Do global change experiments overestimate impacts on terrestrial ecosystems? *Trends in Ecology and Evolution*, *26*(5), 236–241. https://doi.org/10.1016/j.tree.2011.02.011
Li, H., & Sivapalan, M. (2014). Functional approach to exploring climatic and landscape controls on runoff generation: 2 Timing of runoff storm response. *Water Resources Research*, *50*(12), 9323–9342. https://doi.org/10.1002/2014WR016308
Li, H., Huang, M., Wigmosta, M. S., Ke, Y., Coleman, A. M., Leung, L. R., et al. (2011). Evaluating runoff simulations from the Community Land Model 4.0 using observations from flux towers and a mountainous watershed. *Journal of Geophysical Research: Atmospheres*, *116*(D24), n/a-n/a. https://doi.org/10.1029/2011JD016276
Li, H., Wigmosta, M. S., Wu, H., Huang, M., Ke, Y., Coleman, A. M., & Leung, L. R. (2013). A physically based runoff routing model for land surface and earth system models. *Journal of Hydrometeorology*, *14*(3), 808–828. https://doi.org/10.1175/JHM-D-12-015.1
Li, H., Sivapalan, M., Tian, F., & Harman, C. (2014). Functional approach to exploring climatic and landscape controls of runoff generation: 1. Behavioral constraints on runoff volume. *Water Resources Research*, *50*(12), 9300–9322. https://doi.org/10.1002/2014WR016307
Lloyd, J., & Farquhar, G. D. (1994). 13C discrimination during CO2 assimilation by the terrestrial biosphere. *Oecologia*, *99*(3–4), 201–215. https://doi.org/10.1007/BF00627732
Lute, A., & Luce, C. H. (2017). National Forest Climate Change Maps: Your Guide to the Future. Retrieved December 20, 2022, from https://www.fs.usda.gov/rm/boise/AWAE/projects/national-forest-climate-change-maps.html
Meira Neto, A. A., Roy, T., Oliveira, P. T. S., & Troch, P. A. (2020). An Aridity Index-Based Formulation of Streamflow Components. *Water Resources Research*, *56*(9), 1–14. https://doi.org/10.1029/2020WR027123
Merz, R., & Blöschl, G. (2004). Regionalisation of catchment model parameters. *Journal of Hydrology*, *287*(1–4), 95–123. https://doi.org/10.1016/j.jhydrol.2003.09.028
Miles, J. (2014). Tolerance and Variance Inflation Factor. In *Wiley StatsRef: Statistics Reference Online*. John Wiley & Sons, Ltd. https://doi.org/https://doi.org/10.1002/9781118445112.stat06593
Neter, J., Wasserman, W., & Michael, K. H. (1983). John Neter_Applied Linear Regression Models.pdf.
Newman, A. J., Clark, M. P., Sampson, K., Wood, A., Hay, L. E., Bock, A., et al. (2015). Development of a large-sample watershed-scale hydrometeorological data set for the contiguous USA: Data set characteristics and assessment of regional variability in hydrologic model performance. *Hydrology and Earth System Sciences*, *19*(1), 209–223. https://doi.org/10.5194/hess-19-209-2015
Nguyen, M. N., & Choi, M. (2022). Advances in evapotranspiration prediction using gross primary productivity based on eco-physiological constraints. *Hydrological Processes*, *36*(6), 1–19. https://doi.org/10.1002/hyp.14628
Niu, S., Xing, X., Zhang, Z., Xia, J., Zhou, X., Song, B., et al. (2011). Water-use efficiency in response to climate change: From leaf to ecosystem in a temperate steppe. *Global Change Biology*, *17*(2), 1073–1082. https://doi.org/10.1111/j.1365-2486.2010.02280.x
Novick, K. A., Ficklin, D. L., Stoy, P. C., Williams, C. A., Bohrer, G., Oishi, A. C., et al. (2016). The increasing importance of atmospheric demand for ecosystem water and carbon fluxes. *Nature Climate Change*, *6*(11), 1023–1027. https://doi.org/10.1038/nclimate3114
Ol'dekop, E. M. (1911). *On evaporation from the surface of river basins, Trans. Meteorol. Obs.*

804 *Univ. Tartu*. *Transactions on meteorological observations*. Tartu, Estonia.
805 Parish, O. O., & Putnam, T. W. (1977). *Equations for Determination of Humidity from*
806 *Dewpoints and Psychrometric Data*. Edwards, California, US, California, US.
807 https://doi.org/NASA TN D-8401
808 Pastorello, G., Trotta, C., Canfora, E., Chu, H., Christianson, D., Cheah, Y. W., et al. (2020). The
809 FLUXNET2015 dataset and the ONEFlux processing pipeline for eddy covariance data.
810 *Scientific Data*, *7*(1), 225. https://doi.org/10.1038/s41597-020-0534-3
811 Peters, W., van der Velde, I. R., van Schaik, E., Miller, J. B., Ciais, P., Duarte, H. F., et al.
812 (2018). Increased water-use efficiency and reduced CO2 uptake by plants during droughts
813 at a continental scale. *Nature Geoscience*, *11*(10), 744–748. https://doi.org/10.1038/s41561-
814 018-0212-7
815 Pike, J. G. (1964). The estimation of annual run-off from meteorological data in a tropical
816 climate. *Journal of Hydrology*, *2*(2), 116–123. https://doi.org/10.1016/0022-
817 1694(64)90022-8
818 Ponton, S., Flanagan, L. B., Alstad, K. P., Johnson, B. G., Morgenstern, K., Kljun, N., et al.
819 (2006). Comparison of ecosystem water-use efficiency among Douglas-fir forest, aspen
820 forest and grassland using eddy covariance and carbon isotope techniques. *Global Change*
821 *Biology*, *12*(2), 294–310. https://doi.org/10.1111/j.1365-2486.2005.01103.x
822 Robinson, N. P., Allred, B. W., Smith, W. K., Jones, M. O., Moreno, A., Erickson, T. A., et al.
823 (2018). Terrestrial primary production for the conterminous United States derived from
824 Landsat 30 m and MODIS 250 m. *Remote Sensing in Ecology and Conservation*, *4*(3), 264–
825 280. https://doi.org/10.1002/rse2.74
826 Samanta, A., Knyazikhin, Y., Xu, L., Dickinson, R. E., Fu, R., Costa, M. H., et al. (2012).
827 Seasonal changes in leaf area of Amazon forests from leaf flushing and abscission. *Journal*
828 *of Geophysical Research: Biogeosciences*, *117*(1), 1–13.
829 https://doi.org/10.1029/2011JG001818
830 Seibt, U., Rajabi, A., Griffiths, H., & Berry, J. A. (2008). Carbon isotopes and water use
831 efficiency: Sense and sensitivity. *Oecologia*, *155*(3), 441–454.
832 https://doi.org/10.1007/s00442-007-0932-7
833 Sivapalan, M., Yaeger, M. A., Harman, C. J., Xu, X., & Troch, P. A. (2011). Functional model
834 of water balance variability at the catchment scale: 1. Evidence of hydrologic similarity and
835 space-time symmetry. *Water Resources Research*, *47*(2), 1–18.
836 https://doi.org/10.1029/2010WR009568
837 Van Der Sleen, P., Groenendijk, P., Vlam, M., Anten, N. P. R., Boom, A., Bongers, F., et al.
838 (2015). No growth stimulation of tropical trees by 150 years of CO2 fertilization but water-
839 use efficiency increased. *Nature Geoscience*, *8*(1), 24–28. https://doi.org/10.1038/ngeo2313
840 Smallman, T. L., & Williams, M. (2019). Description and validation of an intermediate
841 complexity model for ecosystem photosynthesis and evapotranspiration: ACM-GPP-ETv1.
842 *Geoscientific Model Development*, *12*(6), 2227–2253. https://doi.org/10.5194/gmd-12-2227-
843 2019
844 Smallman, T. L., Moncrieff, J. B., & Williams, M. (2013). WRFv3.2-SPAv2: development and
845 validation of a coupled ecosystem–atmosphere model, scaling from surface fluxes of
846 CO<sub>2</sub> and energy to atmospheric profiles.
847 *Geoscientific Model Development*, *6*(4), 1079–1093. https://doi.org/10.5194/gmd-6-1079-
848 2013
849 Sun, Y., Piao, S., Huang, M., Ciais, P., Zeng, Z., Cheng, L., et al. (2016). Global patterns and
850 climate drivers of water-use efficiency in terrestrial ecosystems deduced from satellite-
851 based datasets and carbon cycle models. *Global Ecology and Biogeography*, *25*(3), 311–

323. https://doi.org/10.1111/geb.12411

Tang, Y., & Wang, D. (2017). Evaluating the role of watershed properties in long-term water balance through a Budyko equation based on two-stage partitioning of precipitation. *Water Resources Research*, *53*(5), 4142–4157. https://doi.org/10.1002/2016WR019920

Thornton, M. M., Shrestha, R., Wei, Y., Thornton, P. E., Kao, S.-C., & Wilson., B. E. (2021). *Daymet: Daily Surface Weather Data on a 1-km Grid for North America, Version 4 R1. ORNL DAAC*. Oak Ridge, Tennessee, USA. https://doi.org/https://doi.org/10.3334/ORNLDAAC/2129

Troch, P. A., Martinez, G. F., Pauwels, V. R. N., Durcik, M., Sivapalan, M., Harman, C., et al. (2009). Climate and vegetation water use efficiency at catchment scales. *Hydrological Processes*, *23*(16), 2409–2414. https://doi.org/10.1002/hyp.7358

Turc, L. (1954). The water balance of soils Relation between precipitation evaporation and flow. *Annales Agronomiques*, 491–569. Retrieved from https://www.scopus.com/inward/record.uri?eid=2-s2.0-84978572377&partnerID=40&md5=30a3f6cb3d0a2d47e8e0530cbb853809

Voepel, H., Ruddell, B., Schumer, R., Troch, P. A., Brooks, P. D., Neal, A., et al. (2011). Quantifying the role of climate and landscape characteristics on hydrologic partitioning and vegetation response. *Water Resources Research*, *47*(8), 1–13. https://doi.org/10.1029/2010WR009944

Walsh, R. P. D., & Lawler, D. M. (1981). Rainfall Seasonality: Description, Spatial Patterns and Change Through Time. *Weather*, *36*(7), 201–208. https://doi.org/10.1002/j.1477-8696.1981.tb05400.x

Wang, D., & Tang, Y. (2014). A one-parameter Budyko model for water balance captures emergent behavior in darwinian hydrologic models. *Geophysical Research Letters*, *41*(13), 4569–4577. https://doi.org/10.1002/2014GL060509

Xiao, J., Sun, G., Chen, J., Chen, H., Chen, S., Dong, G., et al. (2013). Carbon fluxes, evapotranspiration, and water use efficiency of terrestrial ecosystems in China. *Agricultural and Forest Meteorology*, *182–183*, 76–90. https://doi.org/10.1016/j.agrformet.2013.08.007

Xie, X., Li, A., Tian, J., Wu, C., & Jin, H. (2023). A fine spatial resolution estimation scheme for large-scale gross primary productivity ( GPP ) in mountain ecosystems by integrating an eco-hydrological model with the combination of linear and non-linear downscaling processes. *Journal of Hydrology*, *616*(9), 128833. https://doi.org/10.1016/j.jhydrol.2022.128833

Xu, D., Agee, E., Wang, J., & Ivanov, V. Y. (2019). Estimation of Evapotranspiration of Amazon Rainforest Using the Maximum Entropy Production Method. *Geophysical Research Letters*, *46*(3), 1402–1412. https://doi.org/10.1029/2018GL080907

Yang, H., Yang, D., Lei, Z., & Sun, F. (2008). New analytical derivation of the mean annual water-energy balance equation. *Water Resources Research*, *44*(3), 1–9. https://doi.org/10.1029/2007WR006135

Yang, S., Zhang, J., Zhang, S., Wang, J., Bai, Y., Yao, F., & Guo, H. (2020). The potential of remote sensing-based models on global water-use efficiency estimation: An evaluation and intercomparison of an ecosystem model (BESS) and algorithm (MODIS) using site level and upscaled eddy covariance data. *Agricultural and Forest Meteorology*, *287*(July 2019), 107959. https://doi.org/10.1016/j.agrformet.2020.107959

Yang, S., Zhang, J., Han, J., Wang, J., Zhang, S., Bai, Y., et al. (2021). Evaluating global ecosystem water use efficiency response to drought based on multi-model analysis. *Science of the Total Environment*, *778*(9), 146356. https://doi.org/10.1016/j.scitotenv.2021.146356

Yang, Y., Long, D., & Shang, S. (2013). Remote estimation of terrestrial evapotranspiration

without using meteorological data. *Geophysical Research Letters*, *40*(12), 3026–3030. https://doi.org/10.1002/grl.50450

Yao, L., & Wang, D. (2022). Hydrological Basis of Different Budyko Equations: The Spatial Variability of Available Water for Evaporation. *Water Resources Research*, *58*(2), 1–14. https://doi.org/10.1029/2021WR030921

Ye, S., Li, H. Y., Huang, M., Ali, M., Leng, G., Leung, L. R., et al. (2014). Regionalization of subsurface stormflow parameters of hydrologic models: Derivation from regional analysis of streamflow recession curves. *Journal of Hydrology*, *519*(PA), 670–682. https://doi.org/10.1016/j.jhydrol.2014.07.017

Ye, S., Li, H. Y., Li, S., Leung, L. R., Demissie, Y., Ran, Q., & Blöschl, G. (2015). Vegetation regulation on streamflow intra-annual variability through adaption to climate variations. *Geophysical Research Letters*, *42*(23), 10307–10315. https://doi.org/10.1002/2015GL066396

Yu, G., Song, X., Wang, Q., Liu, Y., Guan, D., Yan, J., et al. (2008). Water-use efficiency of forest ecosystems in eastern China and its relations to climatic variables. *New Phytologist*, *177*(4), 927–937. https://doi.org/10.1111/j.1469-8137.2007.02316.x

Yu, L., Zhou, S., Zhao, X., Gao, X., Jiang, K., Zhang, B., et al. (2022). Evapotranspiration Partitioning Based on Leaf and Ecosystem Water Use Efficiency. *Water Resources Research*, *58*(9). https://doi.org/10.1029/2021WR030629

Yu, Z., Wang, J., Liu, S., Rentch, J. S., Sun, P., & Lu, C. (2017). Global gross primary productivity and water use efficiency changes under drought stress. *Environmental Research Letters*, *12*(1). https://doi.org/10.1088/1748-9326/aa5258

Zhang, L., Dawes, W. R., & Walker, G. R. (2001). Response of mean annual evapotranspiration to vegetation changes at catchment scale. *Water Resources Research*, *37*(3), 701–708. https://doi.org/10.1029/2000WR900325

Zhang, L., Hickel, K., Dawes, W. R., Chiew, F. H. S., Western, A. W., & Briggs, P. R. (2004). A rational function approach for estimating mean annual evapotranspiration. *Water Resources Research*, *40*(2). https://doi.org/10.1029/2003WR002710

Zhang, S., Yang, H., Yang, D., & Jayawardena, A. W. (2016). Quantifying the effect of vegetation change on the regional water balance within the Budyko framework. *Geophysical Research Letters*, *43*(3), 1140–1148. https://doi.org/10.1002/2015GL066952

Zhang, S., Yang, Y., McVicar, T. R., & Yang, D. (2018). An Analytical Solution for the Impact of Vegetation Changes on Hydrological Partitioning Within the Budyko Framework. *Water Resources Research*, *54*(1), 519–537. https://doi.org/10.1002/2017WR022028

Zhang, Yahai, & Ye, A. (2021). Would the obtainable gross primary productivity (GPP) products stand up? A critical assessment of 45 global GPP products. *Science of the Total Environment*, *783*, 146965. https://doi.org/10.1016/j.scitotenv.2021.146965

Zhang, Yahai, & Ye, A. (2022). Improving global gross primary productivity estimation by fusing multi-source data products. *Heliyon*, *8*(3), e09153. https://doi.org/10.1016/j.heliyon.2022.e09153

Zhang, Yulong, Song, C., Sun, G., Band, L. E., McNulty, S., Noormets, A., et al. (2016). Development of a coupled carbon and water model for estimating global gross primary productivity and evapotranspiration based on eddy flux and remote sensing data. *Agricultural and Forest Meteorology*, *223*, 116–131. https://doi.org/10.1016/j.agrformet.2016.04.003

Zhou, S., Yu, B., Huang, Y., & Wang, G. (2014). The effect of vapor pressure deficit on water use efficiency at the subdaily time scale. *Geophysical Research Letters*, *41*(14), 5005–5013. https://doi.org/10.1002/2014GL060741

948 Zhou, S., Yu, B., Schwalm, C. R., Ciais, P., Zhang, Y., Fisher, J. B., et al. (2017). Response of
949 Water Use Efficiency to Global Environmental Change Based on Output From Terrestrial
950 Biosphere Models. *Global Biogeochemical Cycles*, *31*(11), 1639–1655.
951 https://doi.org/10.1002/2017GB005733
952

## List of Tables

Table 1: Catchments group based on dominant vegetation cover type.

Table 2: Ameriflux sites used in this study

## List of Figures

Figure 1: Conceptual diagram of GPP-ET relationship scenarios

Figure 2: Catchment data used in this study. The CAMELS dataset along with remote sensing data of GPP and vegetation phenology are processed for 380 catchments across CONUS for 1986-2010.

Figure 3: Study catchments characteristics: a) dominant catchment vegetation cover, b) long-term mean annual ET, and c) long-term mean annual carbon uptake Landsat GPP data. Vegetation cover is classified by Deciduous Broadleaf (DBF), Evergreen Forest (Needle leaf + Broadleaf) (EF), and Mixed Forests (MF), Nonforested catchments with Croplands plus Croplands/Natural Vegetation Mosaic (CL/NVM), Grasslands (GL), and a combination of Savannas, Woody Savannas, and Open/Closed Shrublands (WSSL).

Figure 4: Pearson correlation coefficient between monthly GPP and ET in 1986-2010. Scatterplots of normalized GPP versus normalized ET are also shown for 16 representative catchments distributed across CONUS. "r" and "SI" on the plots are the Pearson's r for GPP- ET and the seasonality index for GPP, respectively. The USGS site numbers and the dominant vegetation types (in parenthesis) are listed on top of each scatterplot.

Figure 5: Spatial map of KGE for 380 catchments during the validation period (2003–2010). The CDF describes the percent of catchments with a KGE value less than or equal to a certain magnitude of interest. The 16 catchments for which the validation-period time series plots are displayed are the same as those in Fig. 4a-p. The USGS site number and validation-period KGE for *function-I*/*function-II* in parenthesis are listed on top of each time series plot. Cumulative Distribution Function (CDF) plot of *function-I* and *function-II* performance over the calibration and validation periods are shown in Fig. 5q.

Figure 6: Spatial patterns for the calibrated *function-II* parameters: a) slope and b) intercept coefficient.

Figure 7: Variations of the calibrated *function-II* parameter values (a, b) and green vegetation fraction (GVF) difference (c) across different vegetation regimes showing their seasonal dynamic relationships.

Figure 8: Relationships between the function-II parameters and the climatic and environmental factors. Spearman's ρ is calculated for the catchments within each vegetation regime (as $\rho_{veg}$) and for all the 380 catchments (as ρ included in the subtitle for each subplot), respectively.

Figure 9: Percent of Explained Variance (EV) by all the predictors shown in Fig. 8 and by the first two principal components (PC1 and PC2) of the predictors for the calibrated parameters: (a) for the parameter **β** and (b) for the parameter **α**.

Figure 10: Verifying the multivariable linear regression formulas for estimating β (a, b) and α (c, d) against the calibrated function-II parameter values. The unit for both calibrated and estimated parameters are gC/m2/mm.

Figure 11: Spatial map of validation period KGE for 380 catchments with estimated *function-II* parameters. The 16 catchments for which the validation-period time series plots are displayed are the same as those in Fig. 4a-p. The KGE is for the entire study period (1986-2010).

Figure 12: Monthly time series of simulated and observed GPP for the selected AmeriFlux sites.

Figure 13: Difference between beta and omega across CONUS (13a) and between vegetation regimes (13b).

Table 1: Catchments group based on dominant vegetation cover type.

| Group | Vegetation type(Count) | Group Name | Count |
|---|---|---|---|
| 1 | Deciduous Broadleaf(89) | DBF | 89 |
| 2 | Evergreen Neadleaf Forest(22)<br>Evergreen Broadleaf Forest(3) | EF | 25 |
| 3 | Mixed Forests(50) | MF | 50 |
| 4 | Croplands(46)<br>Croplands/Natural Vegetation Mosaic(65) | CL/NVM | 111 |
| 5 | Savannas(4)<br>Woody Savannas(45)<br>Open Shrublands(7)<br>Closed Shrublands(3) | WS-SL | 59 |
| 6 | Grasslands(46) | GL | 46 |

1045 Table 2: Ameriflux sites used in this study

| Site ID | Lon | Lat | Vegetation | Start Date | End Date | β | α | KGE | $R^2$ |
|---|---|---|---|---|---|---|---|---|---|
| US-ARM | -97.49 | 36.61 | CL/NVM | 2003-01 | 2020-12 | 1.69 | -0.01 | 0.64 | 0.66 |
| US-Bi1 | -121.50 | 38.10 | CL/NVM | 2016-08 | 2021-12 | 0.74 | 0.73 | 0.3 | 0.87 |
| US-Bi2 | -121.54 | 38.11 | CL/NVM | 2017-05 | 2021-12 | 0.74 | 0.74 | 0.14 | 0.79 |
| US-CF1 | -117.08 | 46.78 | CL/NVM | 2017-05 | 2020-12 | 2.01 | -0.61 | 0.58 | 0.87 |
| US-CF2 | -117.09 | 46.78 | CL/NVM | 2017-05 | 2020-12 | 1.99 | -0.60 | 0.62 | 0.85 |
| US-CF3 | -117.13 | 46.76 | CL/NVM | 2017-06 | 2021-12 | 1.98 | -0.59 | 0.61 | 0.84 |
| US-CF4 | -117.13 | 46.75 | CL/NVM | 2017-06 | 2021-12 | 1.98 | -0.59 | 0.66 | 0.89 |
| US-Ne1 | -96.48 | 41.17 | CL/NVM | 2001-06 | 2020-12 | 2.19 | -0.39 | 0.54 | 0.87 |
| US-Ro1 | -93.09 | 44.71 | CL/NVM | 2004-01 | 2016-12 | 2.79 | -1.20 | 0.61 | 0.76 |
| US-Ro5 | -93.06 | 44.69 | CL/NVM | 2017-01 | 2020-12 | 2.78 | -1.19 | 0.5 | 0.63 |
| US-Ro6 | -93.06 | 44.69 | CL/NVM | 2017-01 | 2021-12 | 2.78 | -1.19 | 0.81 | 0.81 |
| US-Tw3 | -121.65 | 38.12 | CL/NVM | 2013-06 | 2018-05 | 0.77 | 0.79 | 0.31 | 0.87 |
| US-HWB | -77.85 | 40.86 | CL/NVM | 2015-08 | 2018-08 | 2.68 | -0.88 | 0.6 | 0.78 |
| US-Ha1 | -72.17 | 42.54 | DBF | 1991-11 | 2020-12 | 2.90 | -0.97 | 0.58 | 0.83 |
| US-MMS | -86.41 | 39.32 | DBF | 1999-02 | 2020-12 | 2.51 | -0.80 | 0.54 | 0.94 |
| US-MOz | -92.20 | 38.74 | DBF | 2004-06 | 2019-12 | 2.29 | -0.56 | 0.61 | 0.93 |
| US-UMd | -84.70 | 45.56 | DBF | 2007-06 | 2021-12 | 3.10 | -1.26 | 0.61 | 0.94 |
| US-xBR | -71.29 | 44.06 | DBF | 2017-02 | 2021-12 | 2.94 | -0.88 | 0.73 | 0.94 |
| US-GLE | -106.24 | 41.37 | EF | 2005-01 | 2020-09 | 3.36 | -0.93 | -0.1 | 0.57 |
| US-Ho2 | -68.75 | 45.21 | EF | 2002-06 | 2020-12 | 3.03 | -1.11 | 0.46 | 0.73 |
| US-Me2 | -121.56 | 44.45 | EF | 2002-01 | 2020-12 | 2.01 | 0.31 | 0.68 | 0.81 |
| US-NR1 | -105.55 | 40.03 | EF | 1999-01 | 2016-12 | 3.38 | -0.79 | 0.06 | 0.71 |
| US-KFS | -95.19 | 39.06 | GL | 2008-01 | 2019-12 | 2.26 | -0.35 | 0.79 | 0.67 |
| US-KLS | -97.57 | 38.77 | GL | 2012-05 | 2019-12 | 1.79 | -0.07 | 0.65 | 0.59 |
| US-ONA | -81.95 | 27.38 | GL | 2016-05 | 2020-12 | 1.35 | 0.90 | 0.86 | 0.79 |
| US-Ro4 | -93.07 | 44.68 | GL | 2014-01 | 2021-12 | 2.77 | -1.18 | 0.66 | 0.92 |
| US-Sne | -121.75 | 38.04 | GL | 2016-06 | 2020-12 | 0.80 | 0.76 | -0.48 | 0.19 |
| US-Rms | -116.75 | 43.06 | WSSL | 2014-10 | 2020-09 | 2.30 | -0.20 | 0.87 | 0.94 |
| US-Rwe | -116.76 | 43.07 | WSSL | 2003-02 | 2007-09 | 2.27 | -0.21 | 0.16 | 0.88 |
| US-Rwf | -116.72 | 43.12 | WSSL | 2014-06 | 2020-09 | 2.14 | -0.12 | 0.72 | 0.94 |
| US-Jo2 | -106.60 | 32.58 | WSSL | 2010-08 | 2020-12 | 0.69 | 0.65 | 0.49 | 0.36 |
| US-Rws | -116.71 | 43.17 | WSSL | 2014-10 | 2020-09 | 1.61 | -0.02 | 0.73 | 0.67 |
| US-SRC | -110.84 | 31.91 | WSSL | 2008-03 | 2014-06 | 0.39 | 0.97 | -0.14 | 0.56 |
| US-Wjs | -105.86 | 34.43 | WSSL | 2007-05 | 2021-12 | 1.09 | 0.32 | 0.8 | 0.76 |
| US-Mpj | -106.24 | 34.44 | WSSL | 2008-01 | 2020-12 | 1.21 | 0.28 | 0.66 | 0.45 |

1046
1047
1048
1049
1050

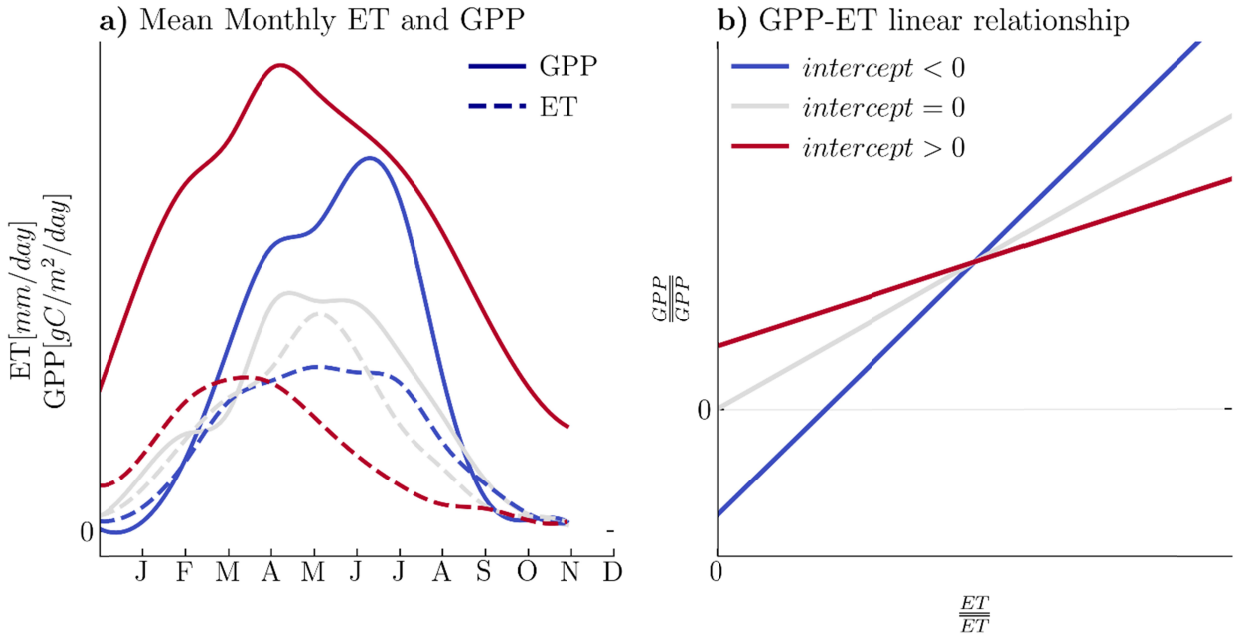


Figure 2: Conceptual illustration of GPP-ET relationship scenarios

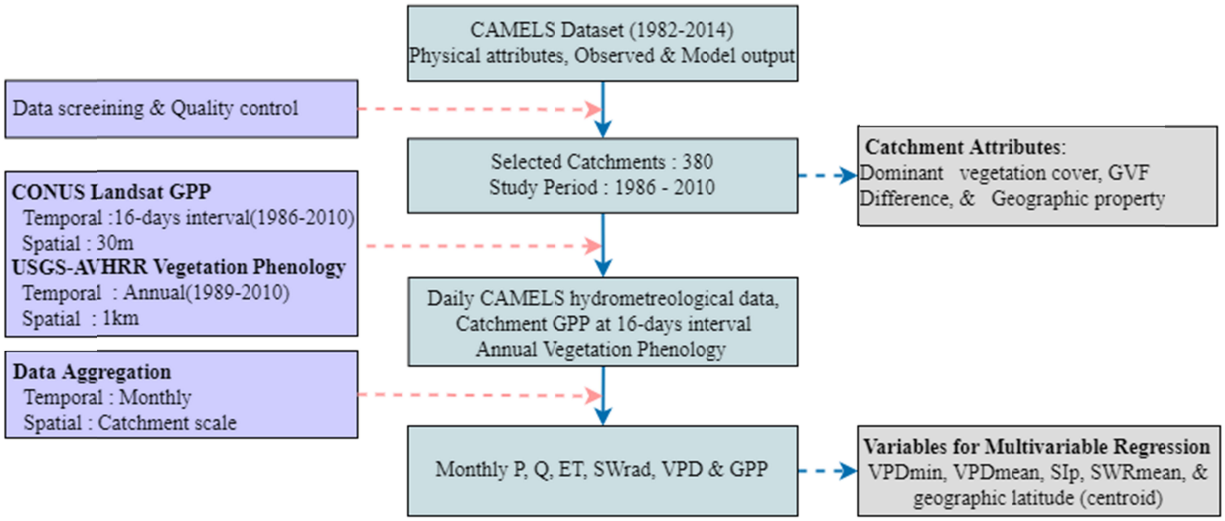


Figure 3: Catchment data used in this study. The CAMELS dataset along with remote sensing data of GPP and vegetation phenology are processed for 380 catchments across CONUS for 1986-2010.

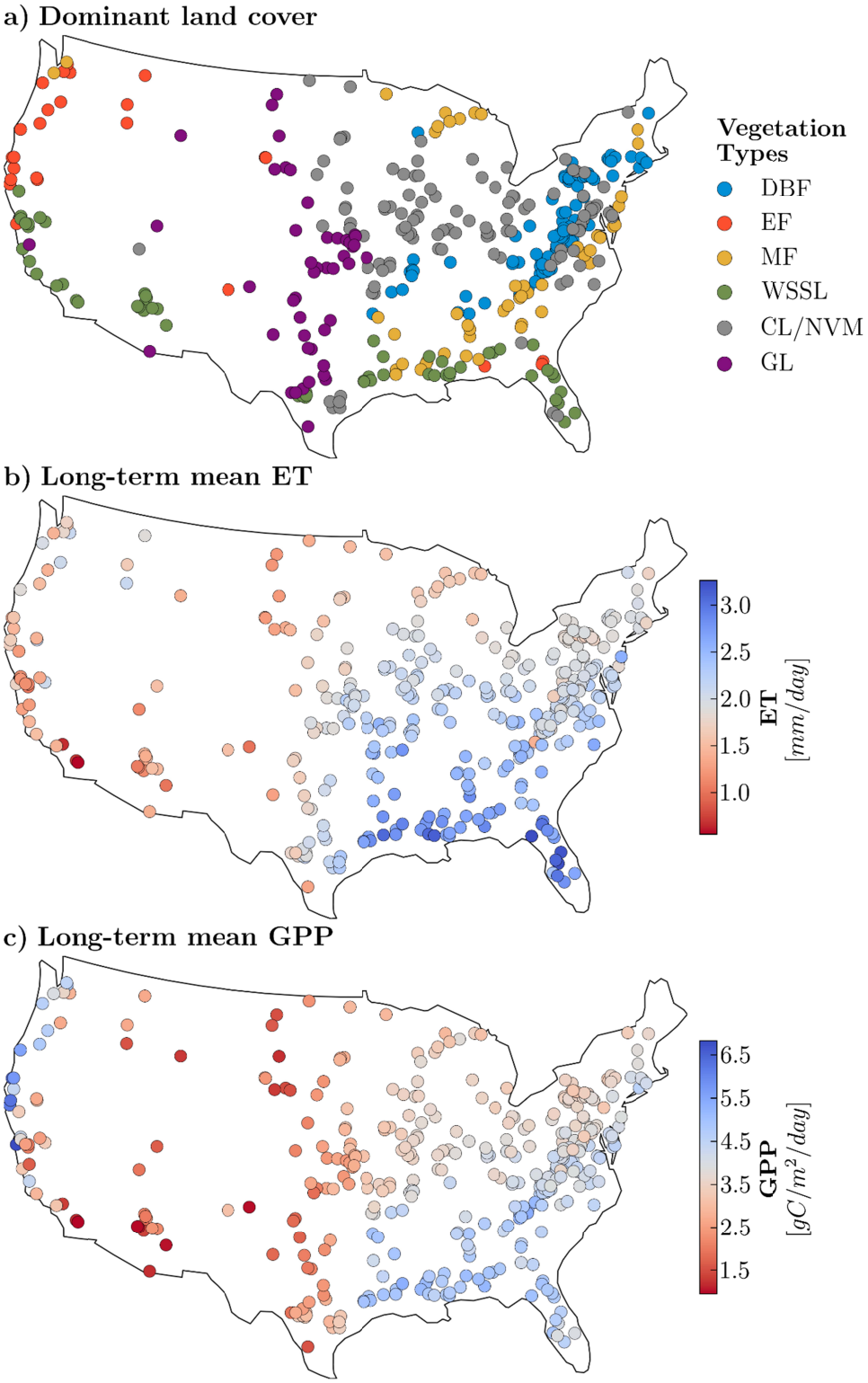


Figure 4: Study catchments characteristics: a) dominant catchment vegetation cover, b) long-term mean annual ET, and c) long-term mean annual carbon uptake Landsat GPP data. Vegetation cover is classified by Deciduous Broadleaf (DBF), Evergreen Forest (Needle leaf + Broadleaf) (EF), and Mixed Forests (MF), Nonforested catchments with Croplands plus Croplands/Natural Vegetation Mosaic (CL/NVM), Grasslands (GL), and a combination of Savannas, Woody Savannas, and Open/Closed Shrublands (WSSL).

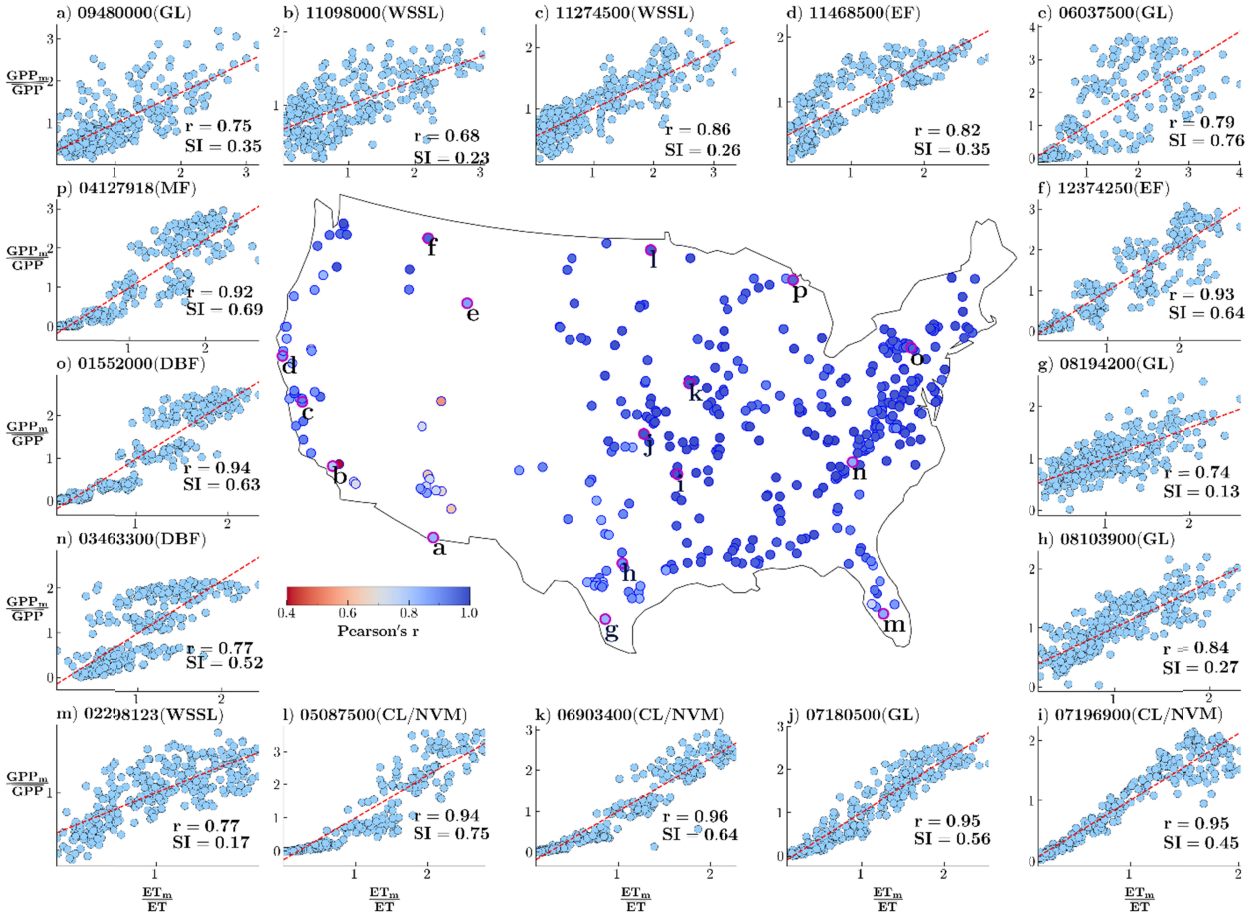


Figure 5: Pearson correlation coefficient between monthly GPP($GPP_m$) and ET ($ET_m$) in 1986-2010. Scatterplots of normalized GPP versus normalized ET are also shown for 16 representative catchments distributed across CONUS. "r" and "SI" on the plots are the Pearson's r for GPP- ET and the seasonality index for GPP, respectively. The USGS site numbers and the dominant vegetation types (in parenthesis) are listed on top of each scatterplot.

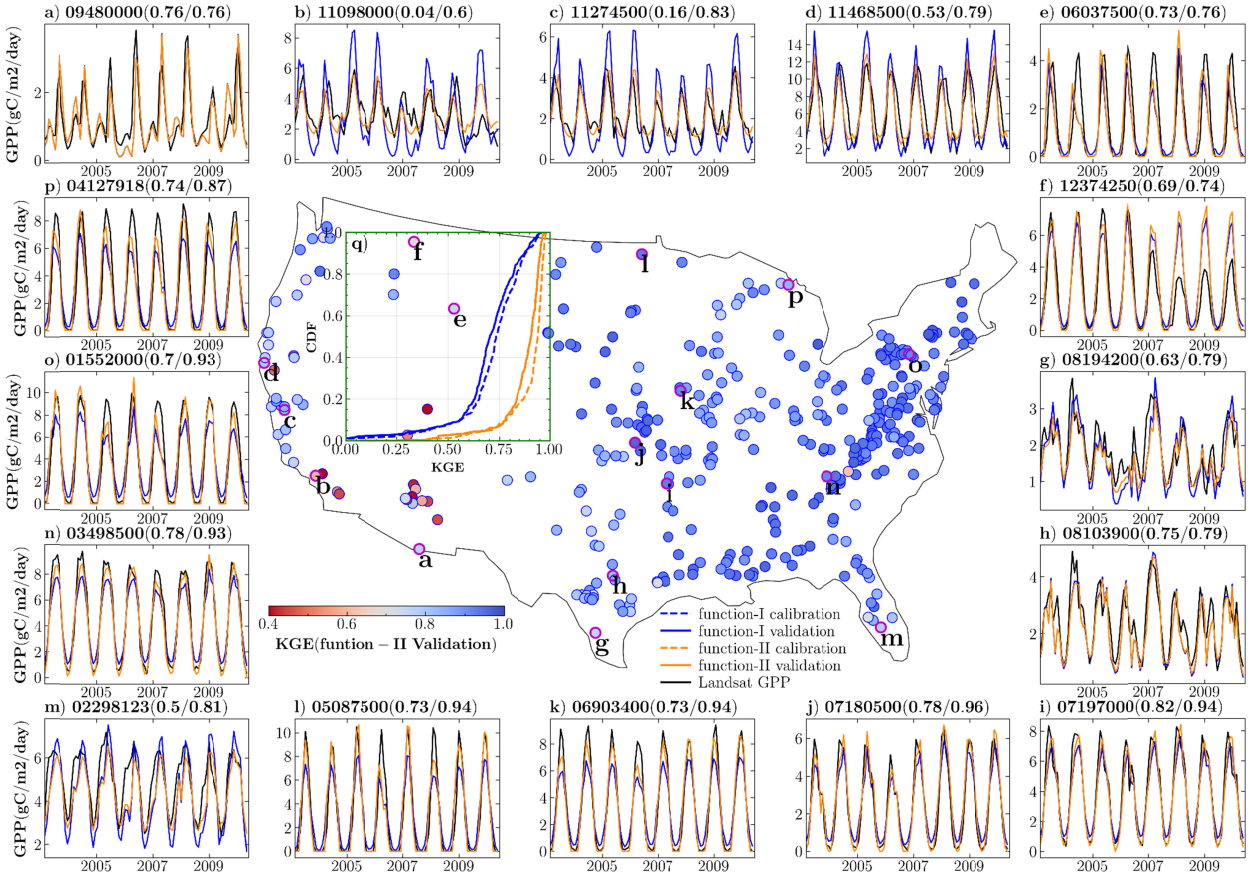


Figure 5: Spatial map of KGE for 380 catchments during the validation period (2003–2010). The CDF describes the percent of catchments with a KGE value less than or equal to a certain magnitude of interest. The 16 catchments for which the validation-period time series plots are displayed are the same as those in Fig. 4a-p. The USGS site number and validation-period KGE for *function-I*/*function-II* in parenthesis are listed on top of each time series plot. Cumulative Distribution Function (CDF) plot of *function-I* and *function-II* performance over the calibration and validation periods are shown in Fig. 5q.

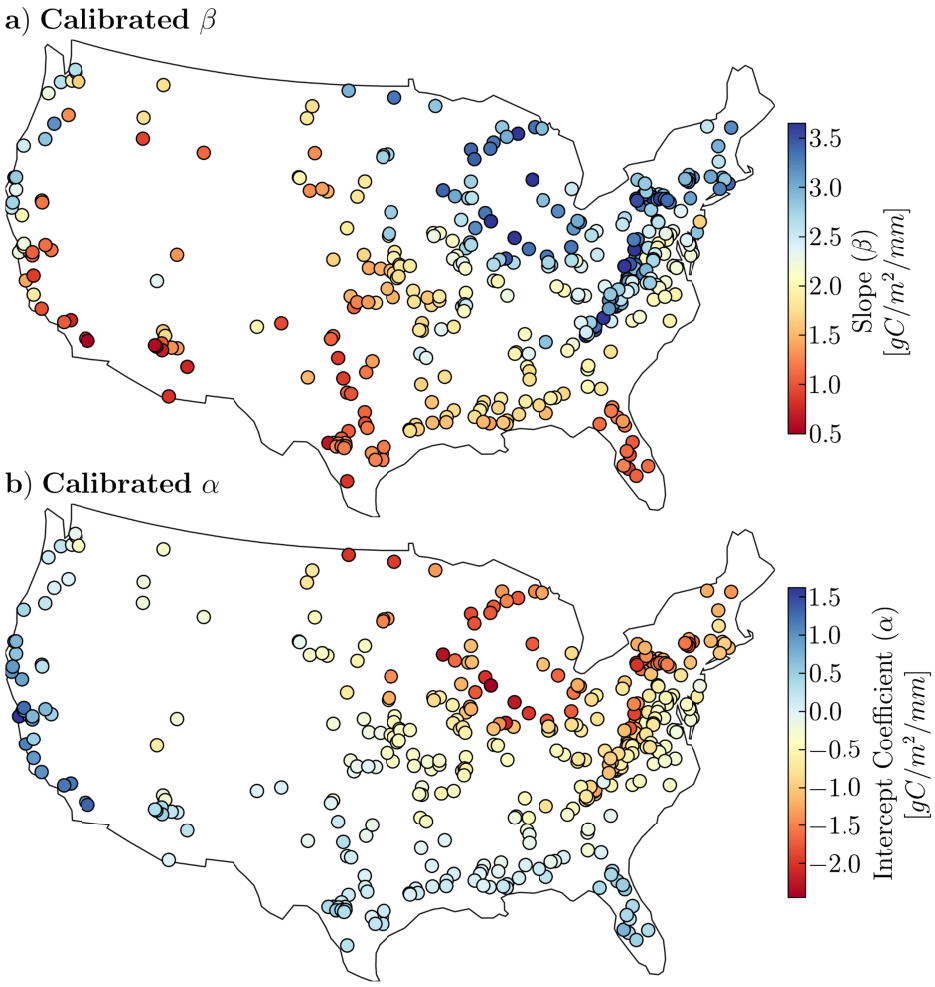


Figure 6: Spatial patterns for the calibrated *function-II* parameters: a) slope and b) intercept coefficient.

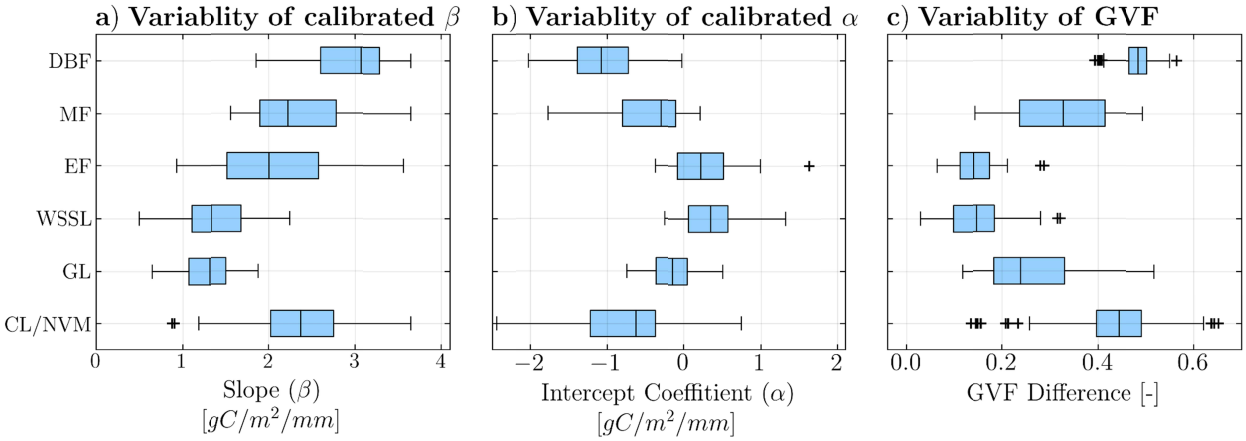


Figure 7: Variations of the calibrated *function-II* parameter values (a, b) and green vegetation fraction (GVF) difference (c) across different vegetation regimes showing their seasonal dynamic relationships.

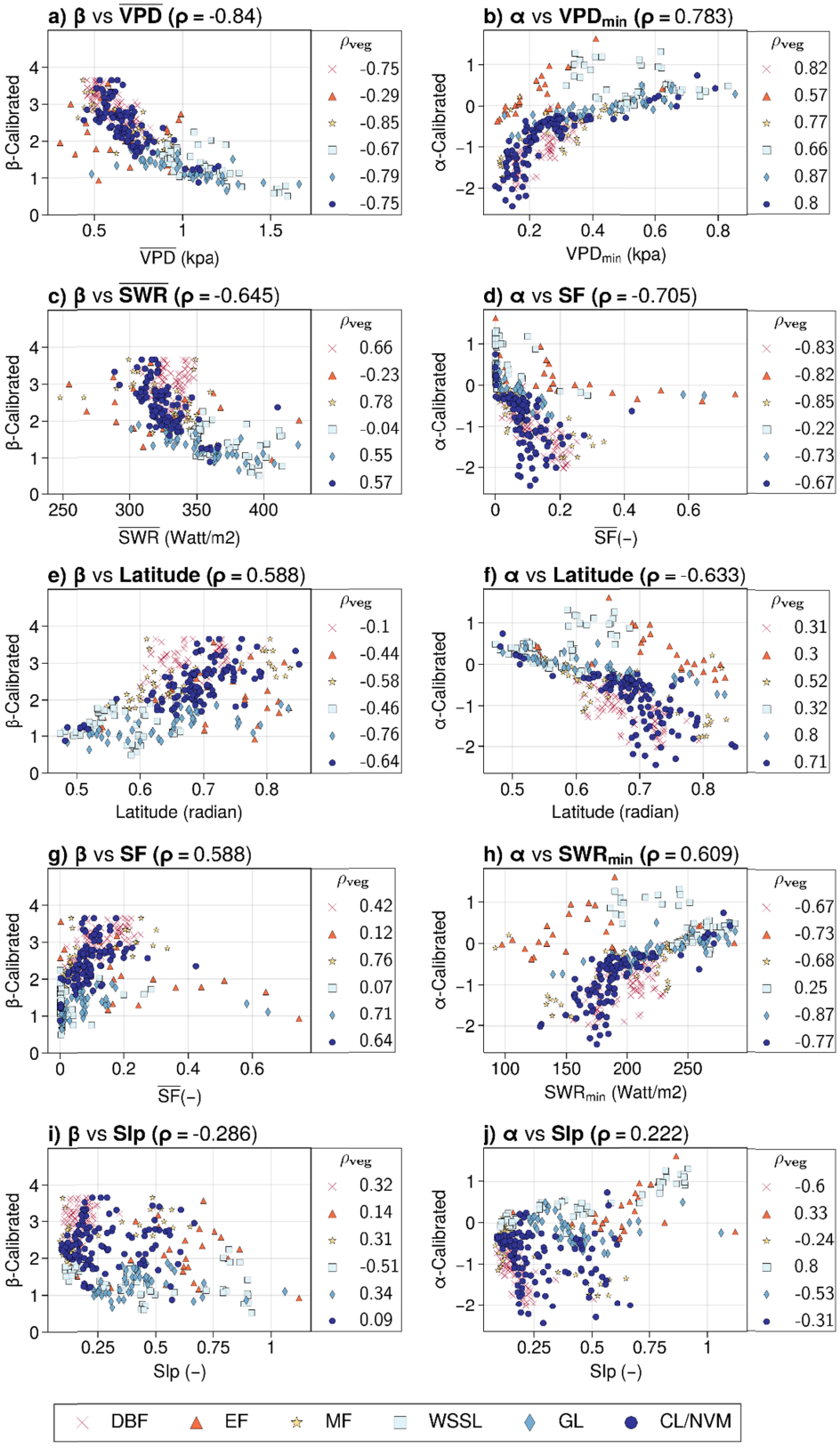


Figure 8: Relationships between the function-II parameters and the climatic and environmental factors. Spearman's ρ is calculated for the catchments within each vegetation regime (as $\rho_{veg}$) and for all the 380 catchments (as ρ included in the subtitle for each subplot), respectively.

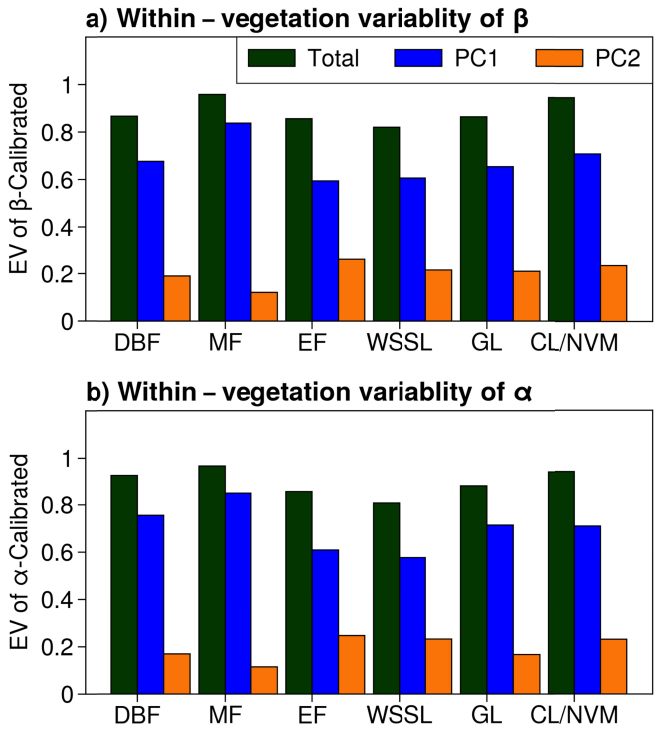


Figure 9: Percent of Explained Variance (EV) by all the predictors shown in Fig. 8 and by the first two principal components (PC1 and PC2) of the predictors for the calibrated parameters: (a) for the parameter β and (b) for the parameter α.

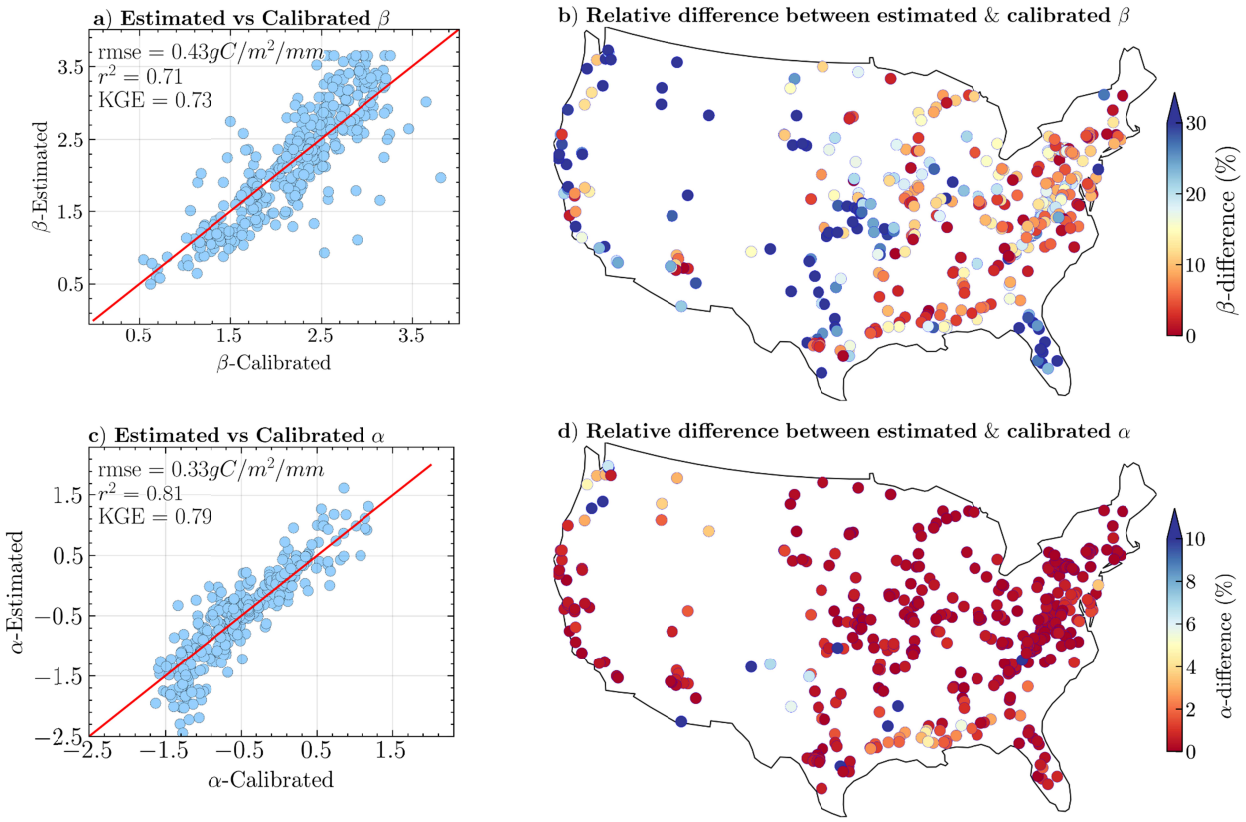


Figure 10: Verifying the multivariable linear regression formulas for estimating β (a, b) and α (c, d) against the calibrated function-II parameter values. The unit for both calibrated and estimated parameters are gC/m2/mm.

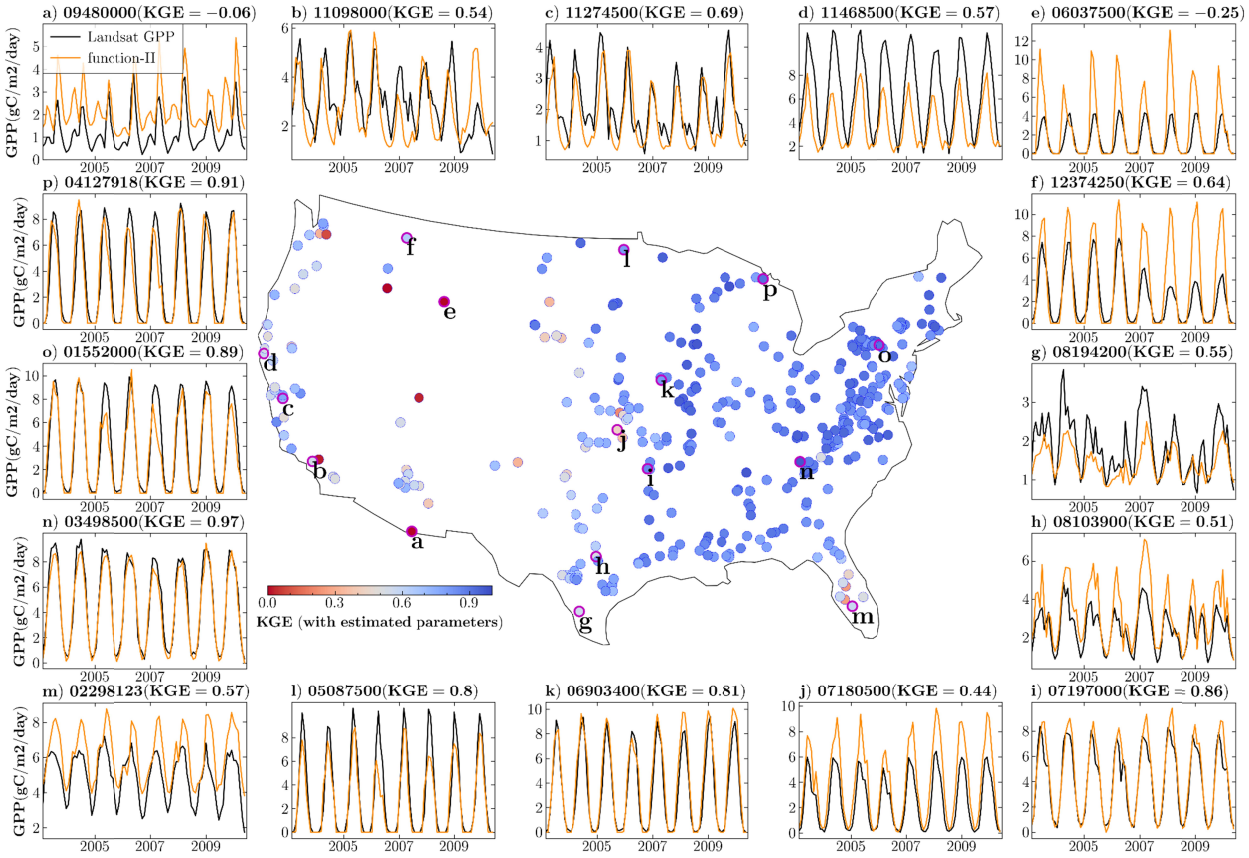


Figure 11: Spatial map of validation period KGE for 380 catchments with estimated *function-II* parameters. The 16 catchments for which the validation-period time series plots are displayed are the same as those in Fig. 4a-p. The KGE is for the entire study period (1986-2010).

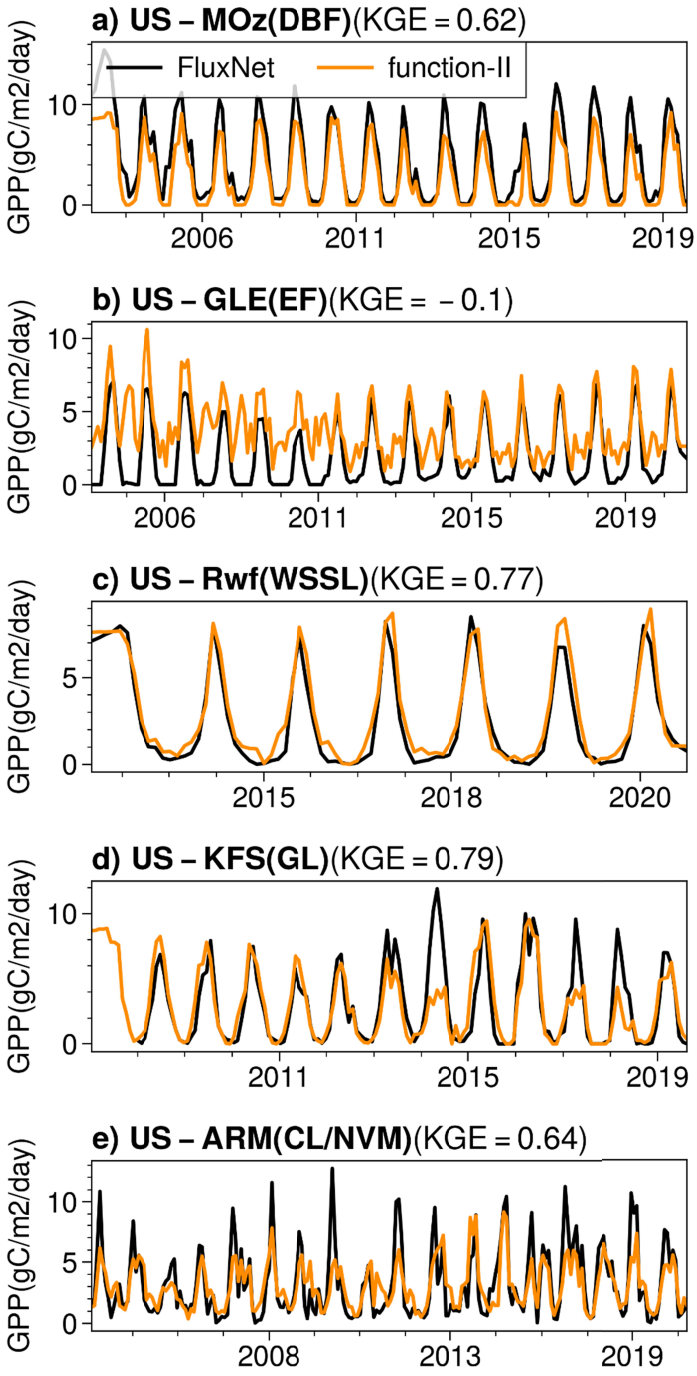


Figure 12: Monthly time series of simulated and observed GPP for the selected AmeriFlux sites.

1274

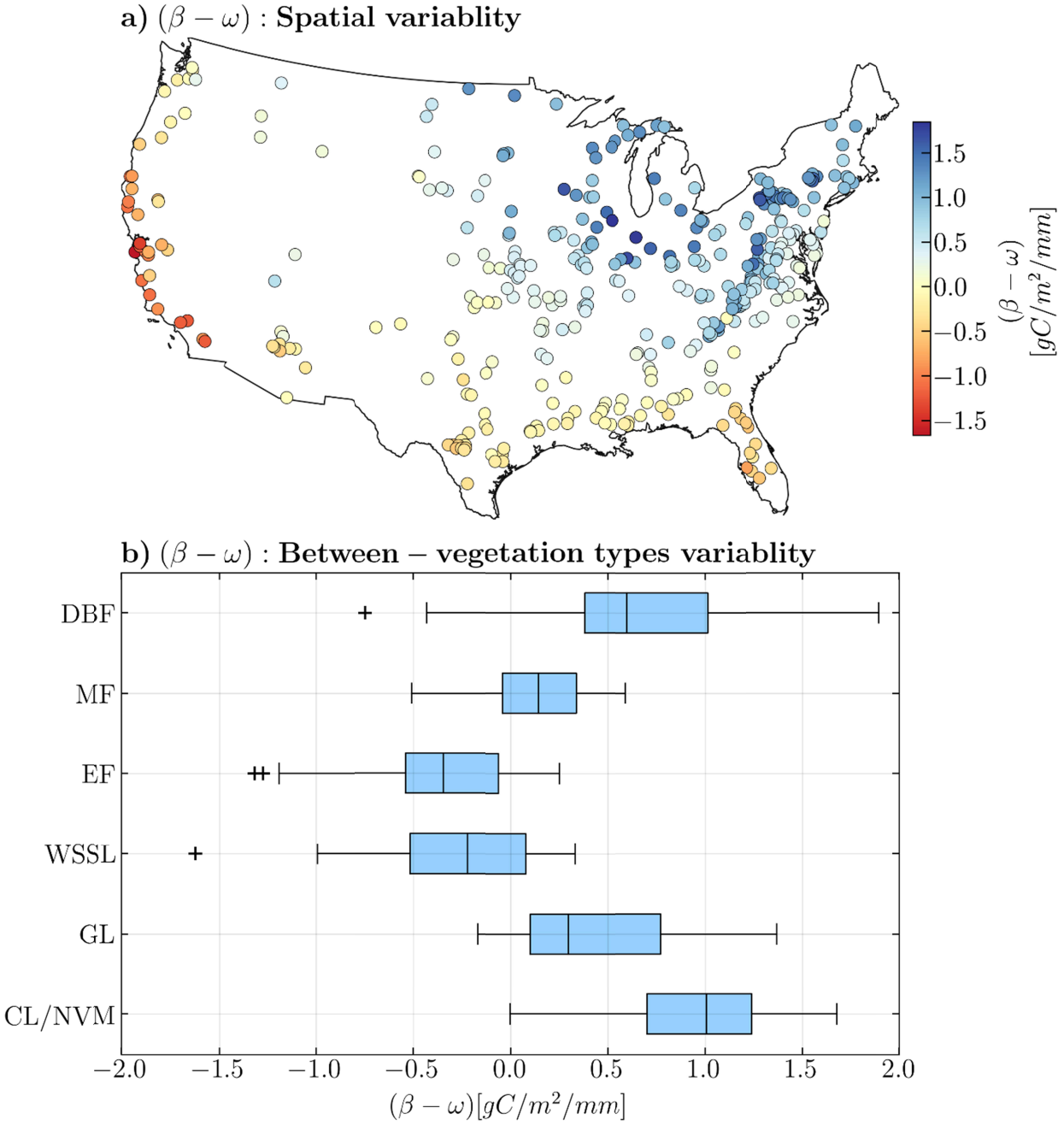


1275
1276
1277 Figure 13: Difference between $\beta$ and $\omega$ across CONUS (13a) and between vegetation regimes
1278 (13b).